Theses and Dissertations   1. Thesis and Dissertation Collection, all items

2019-12

REQUIREMENTS FOR PERUVIAN NAVY SEA INTERDICTIONS USING A UAV-BASED HIGH ENERGY LASER

Canales Herrera, Walter Andres

Monterey, CA; Naval Postgraduate School

http://hdl.handle.net/10945/64118

NAVAL
POSTGRADUATE
SCHOOL

MONTEREY, CALIFORNIA

THESIS

REQUIREMENTS FOR PERUVIAN NAVY SEA INTERDICTIONS USING A UAV-BASED HIGH ENERGY LASER

by

Walter Andres Canales Herrera

December 2019

Thesis Advisor:	Keith R. Cohn
Co-Advisor:	Joseph A. Blau

Approved for public release. Distribution is unlimited.

THIS PAGE INTENTIONALLY LEFT BLANK

REPORT DOCUMENTATION PAGE		*Form Approved OMB No. 0704-0188*

Public reporting burden for this collection of information is estimated to average 1 hour per response, including the time for reviewing instruction, searching existing data sources, gathering and maintaining the data needed, and completing and reviewing the collection of information. Send comments regarding this burden estimate or any other aspect of this collection of information, including suggestions for reducing this burden, to Washington headquarters Services, Directorate for Information Operations and Reports, 1215 Jefferson Davis Highway, Suite 1204, Arlington, VA 22202-4302, and to the Office of Management and Budget, Paperwork Reduction Project (0704-0188) Washington, DC 20503.

1. AGENCY USE ONLY *(Leave blank)*	2. REPORT DATE December 2019	3. REPORT TYPE AND DATES COVERED Master's thesis	
4. TITLE AND SUBTITLE REQUIREMENTS FOR PERUVIAN NAVY SEA INTERDICTIONS USING A UAV-BASED HIGH ENERGY LASER		5. FUNDING NUMBERS	
6. AUTHOR(S) Walter Andres Canales Herrera			
7. PERFORMING ORGANIZATION NAME(S) AND ADDRESS(ES) Naval Postgraduate School Monterey, CA 93943-5000		8. PERFORMING ORGANIZATION REPORT NUMBER	
9. SPONSORING / MONITORING AGENCY NAME(S) AND ADDRESS(ES) N/A		10. SPONSORING / MONITORING AGENCY REPORT NUMBER	
11. SUPPLEMENTARY NOTES The views expressed in this thesis are those of the author and do not reflect the official policy or position of the Department of Defense or the U.S. Government.			
12a. DISTRIBUTION / AVAILABILITY STATEMENT Approved for public release. Distribution is unlimited.		12b. DISTRIBUTION CODE A	

13. ABSTRACT (maximum 200 words)

It is well known that the South Pacific coasts have significant illegal activities such as drug trafficking and forbidden fishing. The government of Peru is concerned about these issues, delegating the responsibility of suppressing the problems to the Peruvian Navy. The Peruvian Navy conducts Maritime Interdiction Operations, and in recent years, specialized patrol boats have been used for easier and more direct interdictions, but they have limited velocity and engagement range. UAV-HEL (Unmanned Aerial Vehicle based High Energy Laser) weapons would overcome those limitations potentially enabling long-range engagements without damaging people or cargo. This research establishes requirements for size, weight and power for a UAV-based HEL to engage and effect damage on a target. Modeling tools are used to estimate irradiance on the target in various Peruvian coastal conditions and engagement geometries to estimate the required dwell time to damage or disable the target. Based on the results, the viability of a UAV-HEL for this application is addressed.

14. SUBJECT TERMS UAV-HEL, interdiction, Peruvian Navy, dwell time, UAV platforms			15. NUMBER OF PAGES 97
			16. PRICE CODE
17. SECURITY CLASSIFICATION OF REPORT Unclassified	18. SECURITY CLASSIFICATION OF THIS PAGE Unclassified	19. SECURITY CLASSIFICATION OF ABSTRACT Unclassified	20. LIMITATION OF ABSTRACT UU

NSN 7540-01-280-5500

Standard Form 298 (Rev. 2-89)
Prescribed by ANSI Std. 239-18

THIS PAGE INTENTIONALLY LEFT BLANK

REQUIREMENTS FOR PERUVIAN NAVY SEA INTERDICTIONS USING A UAV-BASED HIGH ENERGY LASER

Walter Andres Canales Herrera
Ensign, Peruvian Navy
BS, University of Pisa, 2014

Submitted in partial fulfillment of the
requirements for the degree of

MASTER OF SCIENCE IN APPLIED PHYSICS

from the

**NAVAL POSTGRADUATE SCHOOL
December 2019**

Approved by: Keith R. Cohn
Advisor

Joseph A. Blau
Co-Advisor

Kevin B. Smith
Chair, Department of Physics

THIS PAGE INTENTIONALLY LEFT BLANK

ABSTRACT

It is well known that the South Pacific coasts have significant illegal activities such as drug trafficking and forbidden fishing. The government of Peru is concerned about these issues, delegating the responsibility of suppressing the problems to the Peruvian Navy. The Peruvian Navy conducts Maritime Interdiction Operations, and in recent years, specialized patrol boats have been used for easier and more direct interdictions, but they have limited velocity and engagement range. UAV-HEL (Unmanned Aerial Vehicle based High Energy Laser) weapons would overcome those limitations potentially enabling long-range engagements without damaging people or cargo. This research establishes requirements for size, weight and power for a UAV-based HEL to engage and effect damage on a target. Modeling tools are used to estimate irradiance on the target in various Peruvian coastal conditions and engagement geometries to estimate the required dwell time to damage or disable the target. Based on the results, the viability of a UAV-HEL for this application is addressed.

THIS PAGE INTENTIONALLY LEFT BLANK

TABLE OF CONTENTS

THIS PAGE INTENTIONALLY LEFT BLANK

LIST OF FIGURES

THIS PAGE INTENTIONALLY LEFT BLANK

LIST OF TABLES

THIS PAGE INTENTIONALLY LEFT BLANK

ACKNOWLEDGMENTS

I would like to thank the Peruvian Navy for the opportunity to help me grow personally and professionally. I also want to thank Professors Keith Cohn and Joseph Blau, my advisors, for their professional work and their support of my research. Finally, I want to thank my family, especially my wife, Ana; without her unconditional support I would not achieved this goal.

THIS PAGE INTENTIONALLY LEFT BLANK

I.   INTRODUCTION

A.   HISTORY OF ILLEGAL MARITIME ACTIVITIES IN PERU

Peru has been dealing with at least two major illegal maritime activities over the last 20 years: illegal fishing and trafficking of drugs.

The total Peruvian maritime domain, which extends out to 200 nautical miles from its coastline and covers 855,400 square kilometers, is one of the most productive seas around the world. Fishing is the principal economic activity in the sea with nearly five million tons of fish harvested per year, which is between 0.7-1.6% of the Peruvian GNP (Gross National Product) [1]. However, it is also very attractive to make money by fishing without reporting or control. That explains why half of the artisanal fishing ships in Peru have no license to operate. It is not only Peruvian ships that are interested in illegal fishing: there are many foreign ships, most of them from East Asia [2], that operate close to Peru's exclusive economic zone border. This problem is increasing; in 2014, the illegal fishing activity was 25% more than the reports showed and artisanal fishing ships fished 35% more than reported as well. In that context it is estimated that Peru loses S/. 1,200 million ($400 million) every year just from this activity [2].

Additionally, Peru (along with Bolivia and Colombia) is part of the "white triangle," so named for the large amount of illegal drugs (especially cocaine) from those countries that supply Europe and America [3]. Peru, being a coastal country, exports 44% of the illegal drug production by maritime means [4], and the drug traffickers are always innovating different ways for exporting drugs with no detection by using small fast boats that go outside the national maritime domain where they make a cargo transfer to larger boats to transport it overseas. The small fast boats could embark not necessarily from a port but from any point along the coast.

B.   RESPONSIBILITY OF THE PERUVIAN NAVY

The Peruvian government is obligated to fight these illegal activities because they negatively affect the economy and security of the country. The constitutional way to

intervene is by the armed forces, since the military has a mission to "guarantee the sovereignty and to keep the territorial integrity of the State" [5]. The Organic Law of the Peruvian Navy mentions the defense of the seas, rivers, and lakes [6], making the Peruvian Navy the most suitable force for that duty. Additionally, the Peruvian Congress created the Peruvian Coast Guard (Cuerpo de Capitanias y Guardacoastas) as a branch of the Peruvian Navy [7] with the following functions:

- Police fishing activities in seas, rivers, and lakes.

- Control and surveillance of the traffic in jurisdictional areas.

- Port security and surveillance.

- Control and protection of natural resources.

C.   CURRENT METHODS FOR THE PERUVIAN COAST GUARD TO COMBAT THE ILLEGAL ACTIVITIES

The Peruvian Coast Guard is obligated to fight illegal activities at sea; in order to accomplish that duty, the Peruvian Navy conducts Maritime Interdiction Operations (MIO), as defined below:

> Maritime interdiction operation (MIO) is an operation conducted to enforce prohibition on the maritime movement of specified persons or materials within a defined geographic area. MIO are normally restricted to the interception and, if necessary, boarding of vessels to verify, redirect or impound their cargoes in support of the enforcement of economic or military sanctions [8].

The Peruvian Coast Guard published the Maritime Interdiction Operations Manual (MAOPIMA) that establishes the tactical guidance for MIO. This Manual is based on the NATO STANDARD ATP-71 ALLIED MARITIME INTERDICTION OPERATIONS and it shows the steps for a tactical interdiction:

- Detection and surveillance.

- Interrogation, approach, and stopping.

- Boarding and searching.

To detect a target, we have to sense them by some device. Table 1 shows the different sensors that we can use in order to do so:

Table 1.   Sensor Level of Identification. Source: [8].

Sensor	Possible Level of Identification Range (nm)			
	DAY	NIGHT	DAY	NIGHT
Visual	Type: Superstructure Hull colors Name/homeport Suspicious outfit	Type: Superstructure Hull colors Name/homeport	10-15 5-10 <5 0.5-2 <0.5	<5 <2 1-2 <0.5 N/A
Electro-Optical (LLTV)	N/A	Type: Superstructure Hull colors Name/homeport	N/A	5-10 5-10 1-2 <1
Infrared (IRDS/FLIR IR goggles)	N/A	Type: Superstructure Hull colors Name/homeport	N/A	5-10 5-10 1-2 <1
ESM	Radar type	Radar type	RHR	RHR
ESM Fingerprinting	Radar type Name	Radar type Name	RHR	RHR
Imaging radar	Type: Superstructure	Type: Superstructure	64-128 32-64	64-128 32-64
Acoustic (NB)	Noise sources	Noise sources	1-10	1-10
AIS	MMSI, AIS reported information (IMO no., ship name, position, etc.)	MMSI, AIS reported information (IMO no., ship name, position, etc.)	VHF range	VHF range
Radiation	Presence and/or type of radioactivity	Presence and/or type of radioactivity	IAW equipment capabilities	IAW equipment capabilities
Chemical/Biological Agent	Presence and/or type of agent	Presence and/or type of agent	IAW equipment capabilities	IAW equipment capabilities

As the table shows, there are many methods to detect a target. The Peruvian Coast Guard at the moment has only visual, radar, infrared, and Automatic Identification System (AIS) sensing.

D. INTERDICTION LIMITATIONS

The detection during MIO lacks efficiency in some conditions due to intrinsic limitations:

- Limited speed of the naval units to approach the targets.

- The Peruvian Navy lacks jurisdiction at distances more than 200 miles from the coast. Targets near this 200-mile limit often pass over this line as soon as they detect a naval unit.

- Inability to disable potential targets without harming the cargo or crew.

E. POTENTIAL ADVANTAGES OF A UAV-BASED LASER

The speed of potential targets, the inability to easily disable them, and the difficulty in discreetly surveilling them hinders the ability of the Navy to interdict. A UAV-based laser could help in all three areas.

Aerial vehicles are much faster than watercraft, so a potential target cannot outrun a UAV. Furthermore, they can observe targets while flying at high altitudes and from many miles away, so it is less likely such a system will tip off a potential target that they are being surveilled.

There are few ways to stop a boat from air with no damage to the crew and cargo. The ideal option would be to disable the motor in order to allow a naval unit to interdict. This level of precise targeting is possible with a laser weapon.

These advantages make UAV-based lasers worthy of consideration for these kinds of activities.

II. DIRECTED ENERGY OVERVIEW

The idea of a speed of light lethal weapon has been around for a long time. An early suggestion of it is a legend from the Siege of Syracuse (213-212 BC) [9] where the engineer and inventor Archimedes supposedly used bronze mirrors to reflect sunlight to the Roman ship sails in order to burn them. While the technical viability of Archimedes' feat is debated, it is evidence that engineers imagined light as a weapon since ancient times.

This idea was advanced on 22 March 1960 when Townes and Schawlow, under Bell Labs, were granted a US patent for a laser (Light Amplification by Stimulated Emission of Radiation). Since then many researchers have applied this technology for different applications, including military programs such as Navy Laser Weapon System (LaWS), High-Energy Laser with Integrated Optical dazzler and Surveillance (HELIOS), and Solid-State Laser Technology Maturation (SSL-TM).

A. ADVANTAGES / DISADVANTAGES OF DIRECTED ENERGY WEAPONS

Directed energy weapons are getting more interest in the military due to the advantages [10] they have over conventional kinetic weapons; for instance:

- Lethal amounts of energy are delivered with accurate precision, reducing collateral damage.

- Energy is delivered at the speed of light, reducing maneuver opportunities by the target.

- The output power is adjustable to control the level of damage.

- No explosives are required, so they are safer to handle and operate.

- Magazine depth depends only on available power (for non-chemical lasers only).

- A greatly reduced cost per shot (~$1) compared to kinetic weapons (~$1M per missile).

However, there are some disadvantages as well:

- Line of sight to the target is required.

- Finite dwell time is required to accumulate damage.

- If the laser beam misses the primary target, it continues to propagate, possibly placing aircraft and satellites at risk.

- The weather may limit utility. Specifically,

    - Molecules and aerosols absorb and scatter laser light. Also, lasers will not perform as well in fog, haze, rain, etc.

    - Atmospheric turbulence can cause the beam to break apart and/or wander.

    - At high output powers (greater than about 100 kW), thermal blooming can defocus the beam.

B.   LASER WEAPONS OVERVIEW

A laser consists of three main components [11]:

1. A gain medium where the amplification of light takes place; this could be a gas, liquid, solid, or plasma.

2. A power source where energy is supplied to the medium; this source can be, for instance, a flash lamp, an electrical current, or another laser.

3. A feedback mechanism to form an oscillator using an optical cavity, which is a system of two or more mirrors that reflects the light onto itself to provide a feedback mechanism.

In the lasing process, the gain medium is "pumped" to excite the atoms to an upper energy state. Usually, the pumping is obtained from high-intensity light or discharges of electricity to the gain medium to generate an excess of excited-state atoms. When the medium is pumped enough to have more excited-state atoms than ground-state atoms, this is called a population inversion [11]. This process is necessary for a laser to successfully

operate. When the excited atoms return to the ground state, they can release energy in the form of photons with random phase (incoherent light) as shown in Figure 1; this process is called spontaneous emission [11].
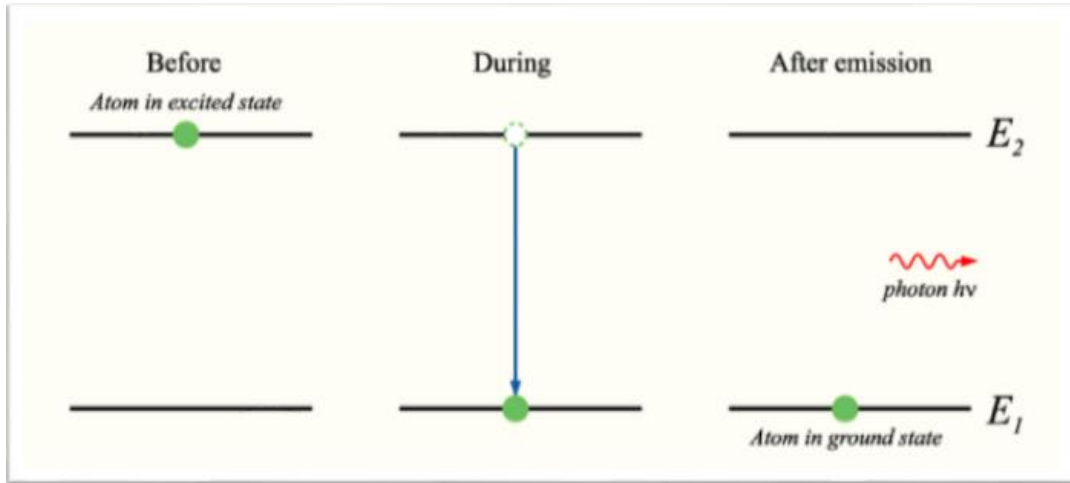
Figure 1.   Spontaneous emission. Source: [10].

However, when the atomic state transitions to the lower level due to the interaction of another photon, the result can be the emission of a photon with the same frequency, phase, and direction as the incident photon (coherent light), as shown in Figure 2; this process is called stimulated emission. Laser light is generated by this process.

$$E_2 - E_1 = \Delta E = h\nu$$
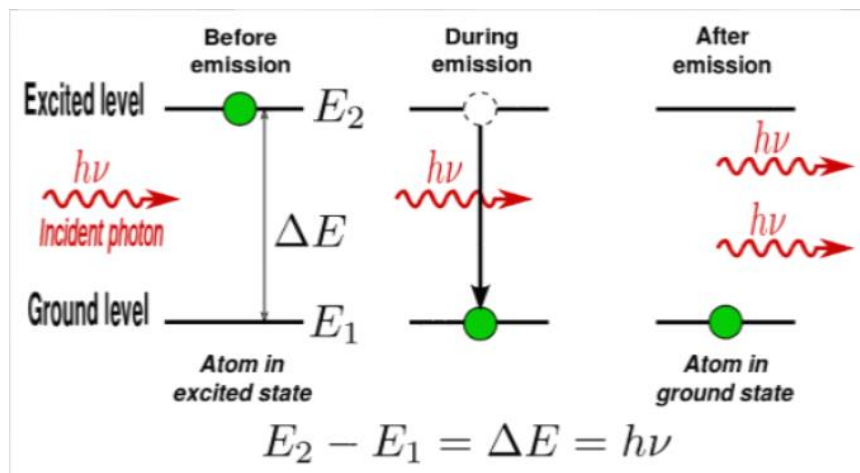
Figure 2.   Stimulated emission. Source: [10].

7

It is essential to point out that spontaneous emission and stimulated emission are both processes that could occur between different atomic energy levels of the laser gain medium. Actually, the overall transitions must occur between three or, more commonly, four levels, depending on the laser, to achieve a population inversion. In the latter case, the lasing process occurs between the third and the second state, as shown in Figure 3.
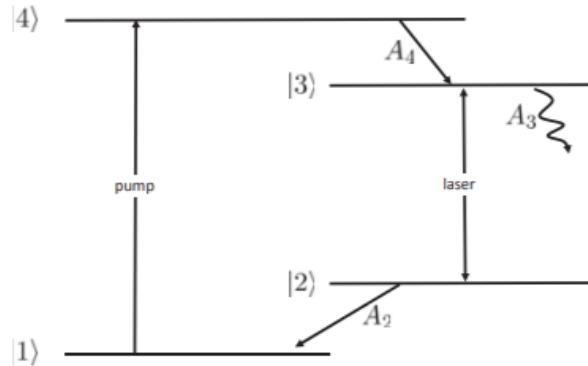
Figure 3.   Configuration of a four-level laser. Source: [11].

C.   LASER WEAPONS PARAMETERS

A target can be damaged by a laser weapon when it focuses a beam of light for a determined period (dwell time) onto a specific target area ("bucket"). The effectiveness of the system depends on various parameters, including the power of the laser (P), the wavelength of the light (λ), the range of the target (R), and the dwell time (τ) [9].

D.   LASER WEAPON TECHNOLOGIES

Various laser technologies have been used for directed energy weapons, including gas dynamic, chemical, free electron, and solid-state lasers.

1.   Gas Dynamic Laser

This type of laser, shown in Figure 4, was "invented by Edward Gerry and Arthur Kantrowitz at Avco Everett Research Laboratory in 1966" [12]. The medium often consists of a combustion chamber, a supersonic expansion nozzle, and carbon dioxide mixed with helium or nitrogen. Gas molecules are heated in the chamber at high temperature and

pressure, exciting vibrational states in order to achieve the population inversion, and later cooled and expanded after passing through the nozzle where molecular vibrational states relax and emit photons. The emitted photons are reflected between the cavity mirrors to provide feedback and enable stimulated emission. A gas dynamic laser's wavelength depends on the type of gas (i.e., CO_2 laser: $\lambda \sim 10.6\ \mu m$).
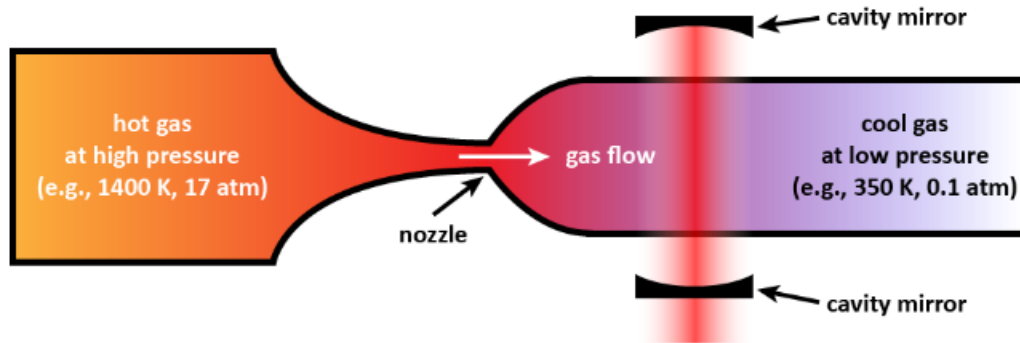
Figure 4.   Gas dynamic laser. Source: [10].

Some advantages of gas dynamic lasers are:

- High power [10];

- Good beam quality [10];

- Waste heat removed with the exhaust [10].

Some disadvantages of gas dynamic lasers are:

- Magazine depth limited by gas supply [10];

- The need to deal with exhaust gases (supersonic, $\sim 170\ °F$) [10];

- Poor propagation in maritime environments due to its wavelength [10].

2.   Chemical Laser

This type of laser was proposed by J.C. Polanyi in 1960 and "demonstrated by J.V.V Kasper and G. Pimentel in 1965" [13] by a flash lamp hydrogen-chlorine explosion. The gain medium consists of chemical delivery systems, a gas generator, and a supersonic

mixing nozzle. Chemicals are delivered into a gas generator to create a multi-chemical gas to be mixed later by the supersonic nozzle, releasing the stored energy from the chemical bond to obtain excited vibration levels. An example of a chemical laser is the Chemical Oxygen Iodine Laser (COIL) shown in Figure 5.
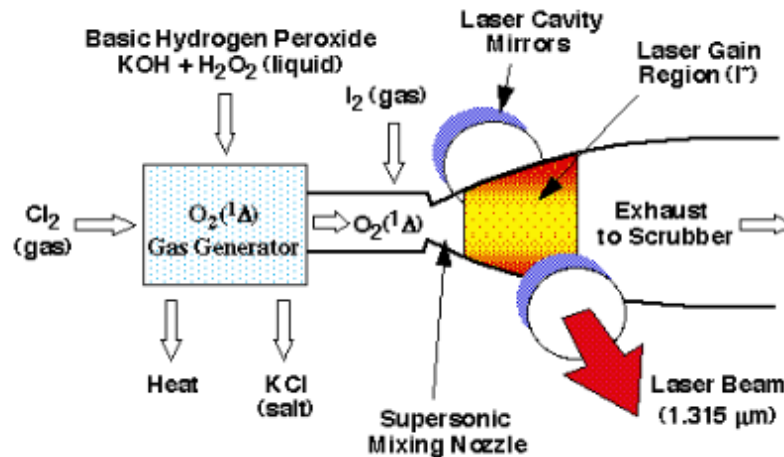
Figure 5.   Chemical oxygen iodine laser. Source: [10].

The lasing wavelength of chemical lasers depends on the type of chemical (i.e., COIL: $\lambda \sim 1.3$ μm).

The advantages of a chemical laser are similar to a gas dynamic laser:

- High power;

- Good beam quality;

- Waste heat removed with the exhaust.

Some disadvantages of chemical lasers are:

- Magazine depth limited by chemical supply;

- Need to deal with laser size;

- Toxic exhaust gases.

3.   Solid-State Laser (SSL)

This laser is based on a solid-state gain medium such as a crystal or glass doped with rare-earth or transition metal ions. After photons are pumped into it by either a flashlamp or another laser, the dopant atoms produce light that bounces between mirrors to facilitate stimulated emission. A basic SSL is shown in Figure 6.
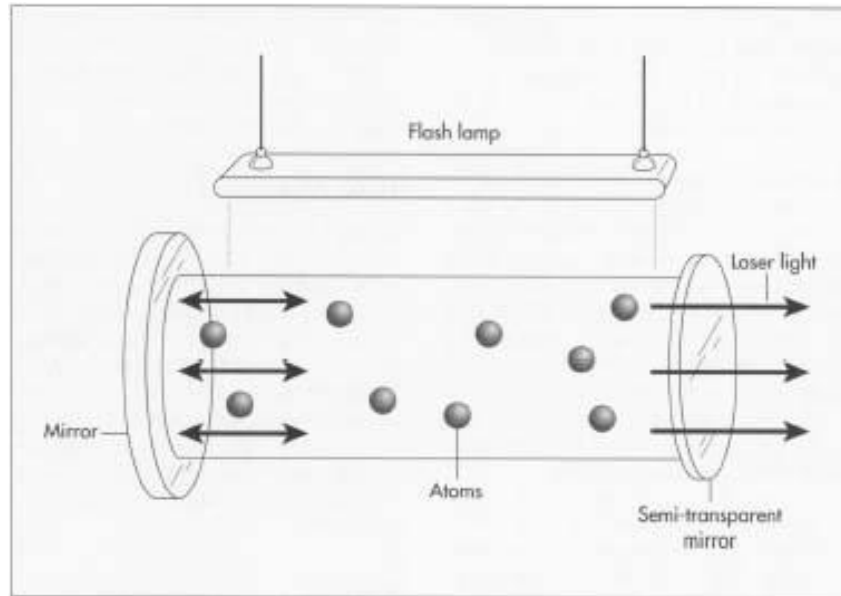
Figure 6.   Solid-state laser. Source: [10].

Solid-state lasers can be further classified by their gain medium geometry: slab, rod, or fiber [9]. Fiber lasers, in particular, have many advantages; for instance:

- The gain medium is flexible, allowing the output to be easily delivered to a movable focusing element, which is important for applications such as laser cutting, welding, and folding of metals and polymers [14].

- High and continuous output power due to the fiber's high surface area to volume ratio, which is important for heat removal [10].

- More compact for the same power output, compared to rod or gas lasers, due to the ability to bend and coil the fiber [10].

11

- Reliability and vibrational stability [10].

- Magazine limited only by available electrical energy [10] (This advantage applies to all solid-state lasers).

However, fiber lasers have a huge disadvantage: they require significant heat removal from the stationary solid-state medium, even with its high surface area to volume ratio. Solid state lasers are also classified by the pumping source: flash lamp or diode-pumped.

a.   *Flash Lamp-Pumped Solid-State Laser*

The pump of this laser consists of a flash lamp, usually xenon, that is surrounded by a reflecting shield that focuses the radiation of the optical pump into the gain medium.

b.   *Diode-Pumped Solid-State Laser*

Diode-pumped lasers need a pump source from another laser; a p-n semiconductor device is usually used to do so. This laser is based on two pumping configurations: (1) an end-pumped arrangement where the radiation from the diode is sent into the end of the solid-state laser rod, and (2) a side-pumped arrangement where the diode radiation is sent into the side of the laser rod.

4.   Free Electron Laser

This laser was invented by John Madey at Stanford University in 1971 using a relativistic electron beam from an accelerator and an undulator, the latter of which consists of a series of magnets with alternating fields. The electrons pass through the undulator at relativistic velocities, where the alternating magnetic fields deflect its path, causing the beam to wiggle and thus emit photons (spontaneous emission). Photons captured by an optical cavity are reflected and amplified by the next pulse sent from the accelerator (stimulated emission). The free-electron laser process is shown in Figure 7.
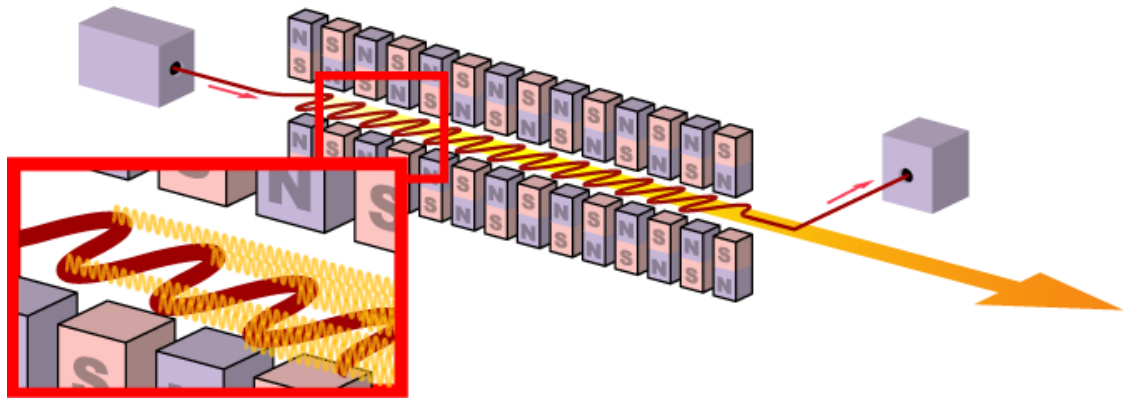
Figure 7.   Free electron laser process. Source: [10].

Some advantages of free electron lasers are:

- Arbitrary wavelength determined by electron beam energy and undulator design.

- Magazine limited only by available electrical energy.

- Waste heat removed at approximately the speed of light.

- Excellent optical beam quality for propagation.

- Size and complexity of the structure do not scale with output power.

Some disadvantages of free electron lasers are:

- They are typically large (~20 m long) and heavy.

- It is a relatively immature technology.

- Shielding is required from radiation produced by the relativistic electron beam.

E.   DIRECTED ENERGY WEAPONS EXAMPLES

In recent years, the U.S. Navy has been developing solid-state laser (SSL) projects in order to defend against threats such as UAVs and small boats. Some of the recent and current programs are discussed below.

1. AN/SEQ-3 Laser Weapon System (LaWS)

"The AN/SEQ-3 Laser Weapon System was built by Kratos. LaWS was deployed on the USS *Ponce* in 2014, integrating it with the vessel's Phalanx close-in weapon system (CIWS), which uses a radar tracking system for targeting and guidance" [15].

It uses a beam with wavelength near one micrometer generated from an array of fiber lasers. This system has a modifiable output power that can be adjusted from high to low output power. "At high output power (around 30kW), the laser can destroy targets, fry sensors, burn out motors and detonate explosive material. At low output power, the LaWS system can dazzle enemy combatants and cause them to turn away from threatening positions" [15].

"The 30-kW LaWS deployed in 2014 to the Persian Gulf was able to shoot down drones and disable small boats, and temporarily blind (or 'dazzle') sensors, as well as use its targeting optics for threat identification" [16]. A photo of LaWS on the USS *Ponce* is shown in Figure 8.

Figure 8.   LaWS on USS *Ponce*. Source: [16].

2. High-Energy Laser with Integrated Optical Dazzler and Surveillance (HELIOS)

"On January 26, 2018, U.S. Navy awarded Lockheed Martin a $150 million contract for the development, manufacture, and delivery of two HELIOS systems—one for installation on a Navy *Arleigh Burke*-class Aegis destroyer, the other for land-based testing" [16].

HELIOS is a multi-function system that consist of three main functions [16]:

- HEL weapon to eliminate threats such as unmanned systems (UAS) and small boats.

- Long-range intelligence, surveillance, and reconnaissance (ISR) capability to provide information in real-time.

- Laser dazzler to disable the ISR ability of UAS.

HELIOS output power is approximately 60 kW, higher than LaWS, but lower than the SSL-TM system.

The biggest challenge for the HELIOS project is to fully integrate into the ship's Aegis combat system and the electrical source of *Arleigh Burke*-class destroyers, which weren't designed with a lot of power to spare. As Rear Admiral Ron Boxall, the Navy's Director of Surface Warfare, said:

> The problem I have today is the integration of that system into my existing combat system. If I'm going to burn the boats, I'm going to replace something I have today with that system doing that mission with these weapons.

3. Solid-State Laser Technology Maturation (SSL-TM)

"The U.S. Navy initiated the SSL-TM program, in which companies such as BAE Systems, Northrop Grumman, and Raytheon competed to develop a shipboard laser with output power up to 150 kW" [16]. This was intended to be a single system that would demonstrate and advance various HEL technologies such as spectral beam combination. It would be a stand-alone system, not directly integrated with the ship's power, combat systems, etc.

In 2015, DoD announced that Northrop Grumman was selected for the SSL-TM project. In January 2018, the Navy announced that the SSL-TM laser will be installed on the USS *Portland* (LPD-27) [16].

The SSL-TM system consists of a laser and beam director, a thermal storage module, an energy storage module, and a display/control system, as shown in Figure 9. The biggest difference between SSL-TM and the previous systems is the development of leading-edge technology rather than current off-the-shelf technology.
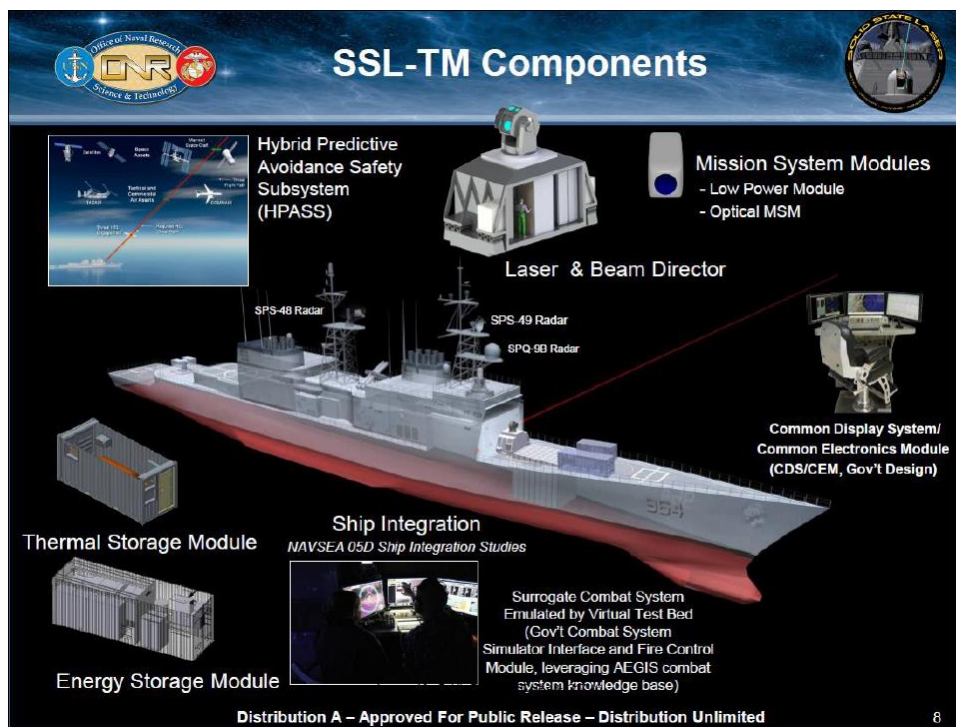
Figure 9.   SSL-TM System. Source: [17].

III. UAV PLATFORMS

A. INTRODUCTION TO UAVS

An aircraft can fly with no onboard pilot and crew by three ways: remotely piloted vehicles (RPVs), drones, and unmanned aerial vehicles (UAVs). An RPV is piloted from a remote position and has no capability to make changes in the flight by itself. A drone is a fixed flight pattern vehicle; consequently, it is not able to accomplish sophisticated missions. A UAV instead is able to perform autonomous or preprogrammed missions making all the changes needed for the current mission.

UAV systems are normally composed of four sub-systems: the air vehicle, the payload, the mission planning and control station (MPCS), and the data link [18]. They also need a launch and recovery system and maintenance equipment, but this chapter will focus only on the operational part of the entire system. A generic UAV system is shown in Figure 10.
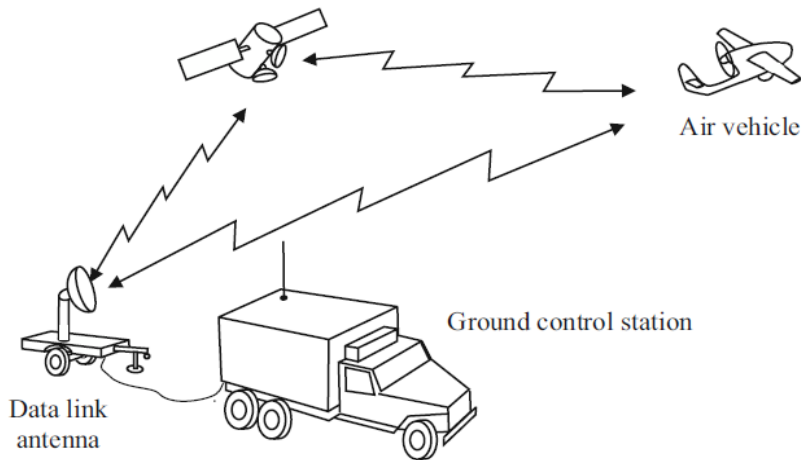
Figure 10.   Generic UAV system. Source: [18].

1. Air Vehicle

UAVs are classified based on the size of the air vehicle.

Very small UAVs: In the range of micro sized (30-50 cm), they usually fly like an insect with flapping wings or like an aircraft with rotary wings. The CyberQuad is an example of a very small UAV as shown in Figure 11.

Figure 11.   CyberQuad. Source: [19].

Small UAVs: Between 50 cm and 2 m, usually with fixed wings and hand-launched by an operator. AeroViroment RQ-11 Raven is an example of small UAV, as shown in Figure 12.

Figure 12.   AeroViroment RQ-11 Raven. Source: [20].

Medium-sized UAVs: These vehicles are large enough to make it impossible for one single person to carry but are still smaller than a light aircraft. Their size is typically between 5 and 10 m and they offer a payload capacity of about 200 kg. Watchkeeper is an example of a medium-sized UAV, as shown in Figure 13.

Figure 13.　Watchkeeper. Source: [21].

Large UAVs: These are often bigger than a light manned aircraft. Their typical size range is larger than 10 m. Such large aircraft usually have enough endurance to fly very long distances away from their base for extended periods of time. Another consideration is to have enough space to carry payloads such as large weapons or sensors. The Global Hawk is an example of a large UAV, as shown in Figure 14.

Figure 14.　Global Hawk. Source: [22].

Regardless of the size, a UAV typically consists of the following subsystems:

- Airframe: The mechanical structure of the aircraft.

- Propulsion unit: The engine in charge of generating thrust.

- Flight controls: All the structure used to maintain aircraft stability.

- Electric power system: The energy source (i.e., batteries) that release power for propulsion and for payload uses.

2. Payload

UAV payloads vary depending on the mission. Missions might include surveillance, target designation, or attack. The payload is considered a sub-system because it is completely independent of the other sub-systems, it is interchangeable between different air vehicles (if the size allows) and it is usually the most expensive of the sub-systems. For surveillance purposes the payload is usually composed of sensors such as video cameras, IR cameras, and/or radar. If target designation is needed, the payload also is composed of a laser designator, often a Moving Target Indicator (MTI), and more rarely an Identifier Friend or Foe (IFF). Finally, for attack missions, we have to add the weapon system, which might be a laser, a missile, or a rocket. Weapon systems usually need power and cooling [18].

3. Mission Planning and Control Station

"MPCS, also called Ground Control Station (GCS), is the operational control center of a UAV system where all the data from the air vehicle is processed and displayed. It is composed of display consoles, video and telemetry instrumentation, communication antennas, pilot and payload operation consoles, work stations, and power supplies" [18]. From MPCS, a mission planner can send the orders to the air vehicle and operate the payload depending on the orders received from headquarters or the staff in charge.

MPCS sizes differ depending on the vehicle, the mission, and the communication range. A station could be as small as a portable backpack that communicates by a remote

control or a large headquarters very far away from the UAV that communicates by satellite systems. A large MPCS is shown in Figure 15.
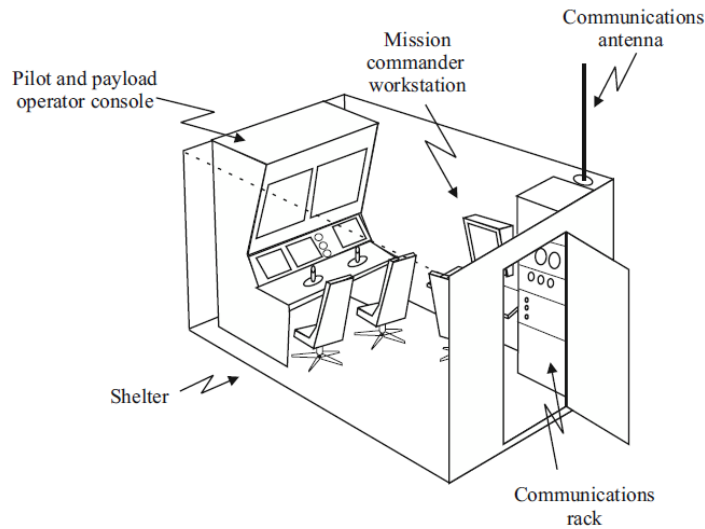
Figure 15.   Mission Planning and Control Station. Source: [18].

4.   Data Link

Data link is basically the interchange of information between an air vehicle and the MPSC at an assigned frequency. It has two phases: upload and download of information. The uplink with a typical data rate of a few KB/s transmits the commands from the MPCS to the air vehicle. The downlink with a typical data rate of 1-10 MB/s transmits the information from sensors and flight status from the air vehicle to the MPCS to be processed and displayed.

B.   UAV EXAMPLES

The following UAVs will be considered for laser platform viability based on their size, payload capacity, flight altitude, and endurance:

1.   Amaru

Amaru is a UAV system developed by the Investigation and Development Center of the Peruvian Air Force (CIDEP). It is an Intelligence, Surveillance and Reconnaissance (ISR) UAV, which could be useful in natural disasters. It can obtain information in real

time from affected areas using an electro-optic camera and an infrared camera through its high frequency transmission antennas [23]. Table 2 shows its characteristics and performance. Amaru is shown in Figure 16.

Table 2.   Amaru characteristics and performance. Adapted from: [23].

Characteristics	Wing Span	23 ft (7.01m)
	Length	17 ft (5.17m)
Performance	Max Altitude	3,281 ft (1,000m)
	Max Endurance	4 hrs

Figure 16.   Amaru UAV. Source: [23].

2.   Predator XP

The Predator XP is the latest UAV system with the Predator name from the General Atomics Aeronautical company. It is designed to operate in many weather conditions such as those found in the Middle East, North Africa, and South America regions. "It is equipped with both Line-of-Sight (LOS) and Beyond-Line-of-Sight (BLOS) data link systems for over-the-horizon operations. It may be integrated with many ISR sensors such as Electro-

Optical Infrared (EO/IR) cameras and multi-mode radars" [24]. Table 3 shows its characteristics and performance. Predator XP is shown in Figure 17.

Table 3.   Predator XP characteristics and performance. Adapted from: [24].

Characteristics	Wing Span	55 ft (17m)
	Length	27 ft (8m)
	Max Gross Takeoff Weight	2,550 lb (1,157kg)
	Fuel Capacity	595 lb (270kg)
	Payload Capacity	325 lb (147kg)
	Power Plant	Heavily Modified Rotax 914 Turbo
Performance	Max Altitude	25,000 ft (7,620m)
	Max Endurance	35 hrs

Figure 17.   Predator XP. Source: [24].

3.   MQ-4C Triton

MQ-4C Triton is an ISR UAV made by Northrop Grumman company built on elements of the Global Hawk UAV while incorporating reinforcements to the airframe and wing. This vehicle is equipped with a mission sensor suite that gives a complete panoramic coverage for all sensors. MQ-4C is able to descend in many weather situations to get a closer view of the target, if needed. [25]. Table 4 shows its characteristics and performance. MQ-4C Triton is shown in Figure 18.

Table 4.   MQ-4C Triton characteristics and performance. Adapted from [25].

Characteristics	Wing Span	130.9 ft (39.9m)
	Length	47.6 ft (14.5m)
	Max Gross Takeoff Weight	32,250 lb (14,628kg)
	Payload Capacity	3200 lb (1,452kg)
	Power Plant	Rolls-Royce AE3007H
Performance	Max Altitude	56,500 ft (17,220m)
	Max Endurance	24 hrs

Figure 18.   MQ-4C Triton. Source: [26].

C.   BATTERIES

Any laser weapon installed on a UAV will need to be power by batteries since the available power on the platform will likely be insufficient to power the weapon.

1.   Overview

The main components of a battery are an anode (the positive terminal), a cathode (the negative terminal), and an electrolyte (a liquid that makes a chemical reaction with the terminals). Once a circuit is built connecting the anode and cathode, it results in a chemical reaction between the anode and the electrolyte. This enables the flow of electrons in two directions: through the circuit and back into the cathode generating a further chemical reaction. When the chemicals inside reach an equilibrium state they will no longer react,

and consequently, the battery would not provide any electric current. For a rechargeable battery, the chemical reaction can be reversed, returning the battery to a fully charged state.

2. Battery Examples

The following battery technologies will be considered for laser power source viability and payload capacity based on their voltage, energy density, maintenance, efficiency, safety and endurance.

a. Lead Acid Batteries

"Lead acid batteries are one of the most commonly used type of battery. Although lead acid batteries have a lower energy density, only moderate efficiency, and higher maintenance requirements than other battery types, they have lower initial costs" [27]. Lead acid batteries have been in use for more than 150 years, making this technology very mature and reliable. There are different kinds of lead acid batteries, including flooded cells and gel cells.

Flooded cells are the original type of lead acid battery and are still commonly used for automobile starter motors. The flooded cells work using an electrolyte of liquid sulfuric acid. They are the most economic lead-acid battery type in terms of cost per amp hour. These cells are also the highest maintenance, requiring watering, charge equalizing, and terminal cleaning.

In a gel cell variety, the electrolyte is suspended with a silica additive causing it to set up or thicken. The ideal working conditions for gel batteries are in very deep cycle applications, providing over a long period of time a constant amount of current. Gel batteries may last a bit longer than flooded cells in hot weather conditions [28].

b. Lithium Ion Batteries

A lithium-ion (Li-ion) battery uses ions of lithium as the vital component of its chemical reaction. This kind of battery provides one of the highest energy densities among any battery technology available today [29]. Li-ion batteries are also comparatively low maintenance.

However, Li-ion batteries tend to overheat over long periods of time, causing damage at high voltage. Under particular conditions this disadvantage can lead to thermal runaway. Li-ion batteries also have to deal with aging, meaning that after some years of operation, they may suffer reduced performance or fail.

c.   *Lithium Iron Batteries*

This is a newer, safer type of rechargeable lithium-ion battery. Its cathode is made up of lithium iron phosphate ($LiFePO4$), and its anodes of carbon. This technology provides improved thermal and chemical stability that results in better safety characteristics than other non-phosphate cathode material lithium-ion batteries. "Lithium phosphate cells are very stable under overcharge or short circuit conditions, they can withstand high temperatures without decomposing" [30], and during charge or discharge period they are incombustible in case of mishandling. Iron and phosphate are cheaper than other cathode materials, so this kind of battery is more economical.

Table 5 shows a comparison sheet for the previous three technologies.

Table 5.   Battery technologies comparison table. Adapted from [31].

BATTERY MODEL	Flooded lead Acid	Lithium-Ion	Lithium Iron
Energy Density (Wh/L)	70-110	200-330	200
Specific Energy (Wh/kg)	30-45	120-160	100
Regular Maintenance	Yes	No	No
Efficiency	100% @20-hr rate 80% @4-hr rate 60% @1-hr rate	100% @20-hr rate 99% @4-hr rate 92% @1-hr rate	100% @20-hr rate 99% @4-hr rate 96% @1-hr rate
Average Cell Voltage	2 V	3.6 V	3.2-3.3 V
Safety	Stable	Not Stable	Stable

IV. ATMOSPHERIC EFFECTS

A. ATMOSPHERE OVERVIEW

The atmosphere is divided into several layers, including troposphere, stratosphere, mesosphere, and thermosphere. The most relevant difference between them is the change of temperature with height. The temperature tends to decrease with height in layers where air molecules have a high transmission to solar energy and increase with height in layers where molecules absorb solar radiation [9]. Figure 19 shows the first four layers.
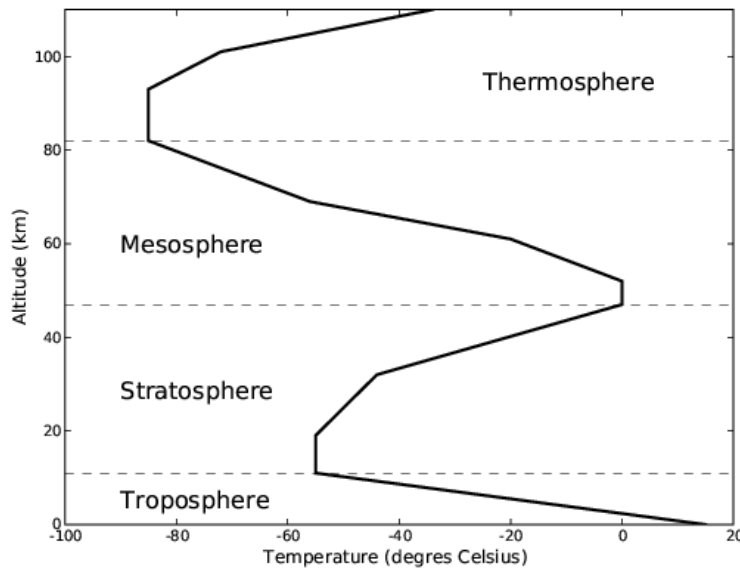
Figure 19.   Layered structure of atmosphere

The most relevant layer in terms of effects on laser weapons systems and UAVs is the troposphere. The troposphere extends from the Earth's surface up to approximately 8 to 18 km, depending on the latitude and season. This layer is the densest in the atmosphere. Within this layer, the temperature decreases approximately linearly with altitude from about 15 °C to -52 °C. Almost all weather and meteorological phenomena occur in this region.

27

The troposphere, in turn, has another layer generated by frictional interaction between wind and the surface of earth called the boundary layer (BL). Its thickness depends on the time of the day: during the day, thickness expands to about $1.5 - 2$ km, while at night it contracts to around 200 m. A relevant BL feature is its well-mixed nature. Thus, the temperature, the water vapor mixing ratio, and the aerosol/pollutant number concentration are all nearly constant with height within the BL. The first 50 meters above the surface of earth is known as the surface layer. While the BL is well-mixed and has a neutral rate of change, in the surface layer the amount of change with height can still be significant.

B.   PRINCIPAL EFFECTS

1.   Absorption and Scattering

Absorption and scattering are two primary ways light from a laser beam can interact with the atmosphere. When a photon encounters an air molecule or an aerosol particle, the photon can be absorbed by the particle or be scattered in a random direction; in both of these cases, some light is removed from the beam, reducing the power hitting the target [33].

Those interactions will depend on the effective cross-section and number density of the particles along the path. The cross-section is given by

$$\sigma = \pi \ r^2,$$

where r is the effective radius of the air particle (where a larger r corresponds to a more probable interaction). The number of particles is given by

$$N \ = \ n \ (A \ dz),$$

where n is the particle number density, A is the cross-sectional area where light is passing through, and dz is a distance along the light beam path, as shown in Figure 20. The cross-section for a single atmospheric species will be different for absorption and scattering.
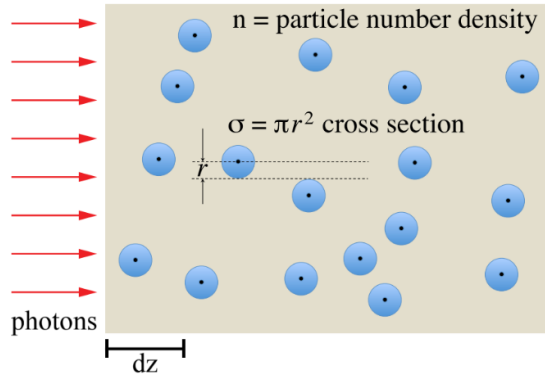
Figure 20.   Photons scattering from particles represented by hard spheres of radius r. Source: [32].

The probability of a photon interacting with a particle is equal to the ratio of the scattered (and/or absorbed) power dP to the total power P in the beam. This ratio is equal to the fraction of the cross-sectional area of the beam that is "blocked" by the particles

$$\frac{dP}{P} = -\frac{\sigma N}{A} = -\sigma n \, dz,$$

where the minus sign indicates that power is being removed from the beam. This differential equation can be integrated to obtain a relationship called Beer's law

$$P(z) = P(0)e^{-\int \varepsilon z},$$

where ε is the extinction coefficient

$$\varepsilon = \sigma \, n.$$

The total extinction coefficient is due to contributions of absorption and scattering from all the types of particles in the atmosphere. We can group these as:

$$\varepsilon = \alpha_m + \beta_m + \alpha_a + \beta_a,$$

where α and β represent the absorption and the scattering, respectively, and a and m represent the molecules (i.e., O_2, N_2, H_2O, etc.) and the aerosols (i.e., smoke, dust, and fog), respectively. These coefficients, especially the molecular components, depend on the

wavelength λ, making the extinction coefficient a function of the wavelength, as shown in Figure 21.
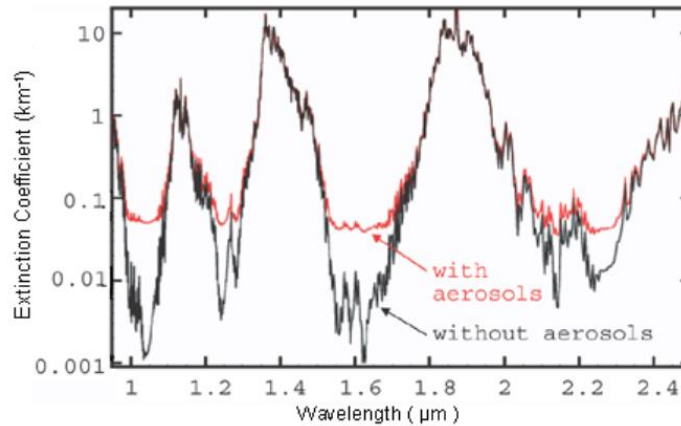
Figure 21. Atmosphere absorption and scattering spectrum. Source: [32].

It is relevant to note that the vertical axis of Figure 21 has a logarithmic scale, meaning that the extinction coefficient can be orders of magnitude lower in some ranges of wavelength (windows). This fact is essential for many applications, including directed energy weapons. Most solid-state directed energy lasers operate in the wavelength window centered near one micrometer.

2.   Turbulence

Atmospheric turbulence can be understood as the contribution of many different scales of motion. The largest are of planetary scale, which constitute most near-continent size weather systems. Mesoscale systems are due to the medium-size atmospheric phenomena such as tropical cyclones and massive thunderstorms. The smallest are the microscale flows, which are mostly contained within the boundary layer and the clouds [32].

Microscale turbulence is characterized by small cells or "eddies" of air with random variations of temperature and humidity, which in turn cause fluctuations of the density and therefore index of refraction of the air. As a consequence, the rays of light traveling through the air are perturbed, causing variations of phase across the wave front, as we observe in Figure 22.
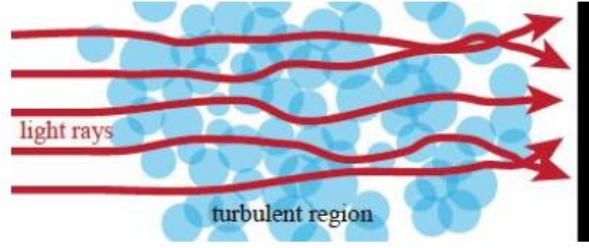
Figure 22.   Ray path perturbation due to turbulence. Source: [32].

Phase changes, when propagating through space, lead to changes in the intensity of the light beam, which can lead to defocusing and breaking up of the beam as it propagates. Microscale turbulence as it applies to visible and near-IR propagation is called "optical turbulence," and is especially prominent in the boundary layer.

As the complexity of representing this physical phenomenon with an exact mathematical model is enormous, we instead describe the severity of turbulence using a statistical parameter called the refractive-index structure (C_n^2) function

$$C_n^2 = \frac{\langle [n(\mathbf{r}) - n(\mathbf{r} + \Delta \mathbf{r})]^2 \rangle}{|\Delta \mathbf{r}|^{2/3}}.$$

Here, $n(\mathbf{r})$ is the index of refraction at point $\mathbf{r}$, $n(\mathbf{r} + \Delta \mathbf{r})$ is the index of refraction a displacement $\Delta \mathbf{r}$ away, and the brackets $\langle ... \rangle$ represents an ensemble average, as shown in Figure 23. According to the Kolmogorov theory of turbulence, this parameter should be constant over a wide range of length scales for a given set of atmospheric conditions.
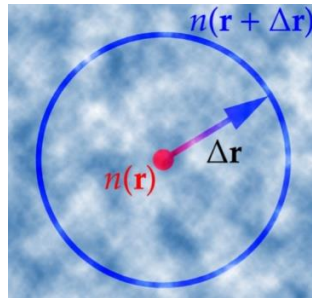
Figure 23.   Eddie of air representation.

Generally, values for this constant are approximately 10^{-18} m$^{-2/3}$ for very weak turbulence and 10^{-13} m$^{-2/3}$ for much stronger turbulence [33], as illustrated in Figure 24.
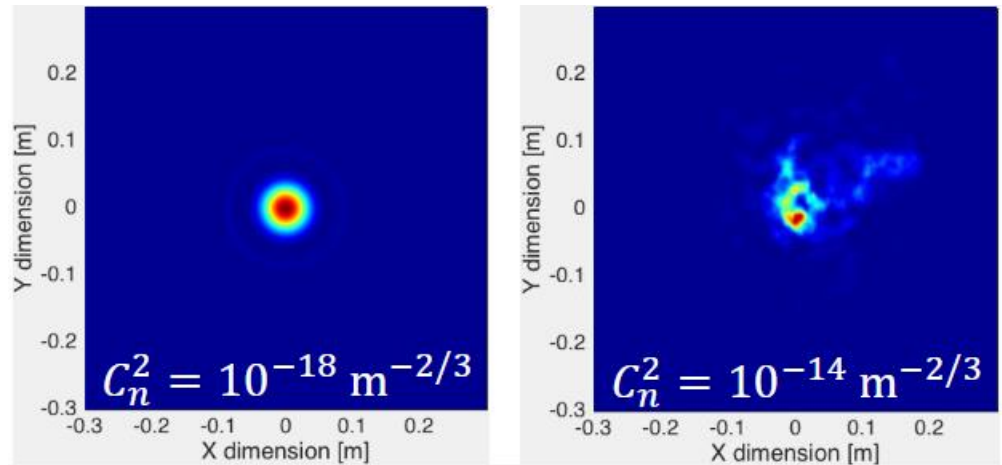
Figure 24. Effect of weak turbulence (left) and strong turbulence (right) on
the laser spot on a target after propagating through the
atmosphere over a distance on 1 km. Source: [32].

The C_n^2 value varies as a function of altitude, rapidly decreasing with altitude near the surface.
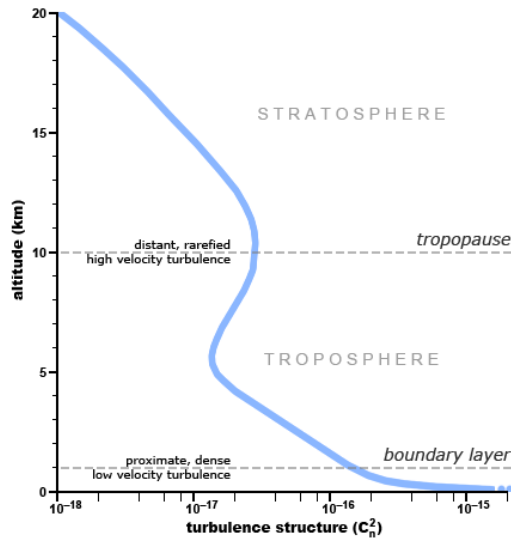
Figure 25. Hufnagel-Valley turbulence model. Source: [32].

The refractive-structure parameter has been measured at numerous sites and altitudes worldwide and parametric estimates are available. One commonly used model is the Hufnagel-Valley model (see Figure 25), which estimates C_n^2 as a function of height h above the ground

$$C_n^2(h) = 5.94 * 10^{-53} \left(\frac{W}{27}\right)^2 h^{10} e^{-\frac{h}{1000}} + 2.7 * 10^{-16} e^{-\frac{h}{1500}} + A e^{-\frac{h}{100}},$$

where h is height in meters, W is the high-altitude wind speed, and A is the C_n^2 at the surface. Typical values for W is 21 m s^{-2} and for A is 1.7 x 10^{-14} m$^{-2/3}$. This particular profile case is known as Hufnagel-Valley 5/7 or HV 5/7.

3.   Thermal Blooming

Thermal blooming happens because of atmospheric absorption. The air molecules increase their temperature as they absorb energy, which changes the air density and hence the index of refraction of the air. These changes make the region act as a lens that de-focuses the laser beam, causing it to spread, thus reducing irradiance on the target. Thermal blooming is relevant at high output powers (≥ 100kW), but could be considered negligible for UAV-based lasers.

THIS PAGE INTENTIONALLY LEFT BLANK

V. TARGET DAMAGE PHYSICS

This chapter will explain how temperature changes within a material over time due to the heat flow generated by an electromagnetic radiation source such as a high energy laser (HEL). This chapter will summarize chapter three of LTJG Carlos Romero's thesis [34], which explains the same concepts for a one-dimensional model. A three-dimensional model will be discussed in the following chapters.

A. LASER HEATING OF MATERIALS AND CONDUCTIVE LOSSES

When the energy from any radiation source hits an object, this energy will be partially absorbed according to the material properties of the object. The energy is conducted as heat and flows from the surface into the material, generating an increase of temperature through the material. This process is described by the heat-flow equation

$$\frac{dT(\vec{r},t)}{dt} = \frac{k}{\rho c_p} \nabla^2 T + \frac{S(\vec{r})}{\rho c_p},$$

where $T(\vec{r},t)$ is the three-dimensional, time-dependent temperature profile of the material, k is the thermal conductivity of the material, ρ is the density of the material, c_p is the specific heat of the material, $S(\vec{r})$ is the source term of the target (power input per unit volume), and $\nabla^2 T$ is the Laplacian of the temperature profile. In this case, the change of phase is not considered yet and k, ρ, and c_p are considered constant within the material.

The source term depends on the irradiance applied to the target, the optical absorption coefficient of the target, and the reflectance of the target. For metallic materials, the energy is absorbed in the first few nanometers, so we will not consider the source term beyond the surface $(x > 0)$ [35]

$$S(x) = \begin{cases} \alpha I(1-R) & x = 0 \\ 0 & x > 0' \end{cases}$$

where α is the optical absorption coefficient of the material, I is the peak irradiance delivered by the HEL to the target, R is the fraction of the optical power that is reflected

by the target, and x is the depth into the material. Here it is assumed that the shape of the laser spot at the target is a uniform ("flat-top") profile.

As mentioned before, the analysis in this chapter will be one-dimensional (where the x-direction is into the target) and will also assume a semi-infinite slab of material. In that case, we can obtain the following analytic solution of the heat-flow equation [35]

$$T(x,t) = T_0 + \frac{2\alpha I(1-R)}{k}\sqrt{Dt}\ \text{ierfc}\left[\frac{x}{2\sqrt{Dt}}\right],$$

where T_0 is the ambient temperature of the air, D is the thermal diffusivity of the material $(D = k/\rho c_p)$, and t is the time. The function ierfc defined by [35] is

$$\text{ierfc}(x) = \int_x^\infty \text{erfc}(\xi)d\xi,$$

with

$$\text{erfc}(x) = 1 - \text{erf}(x) = 1 - \frac{2}{\sqrt{\pi}}\int_0^x e^{-t^2}\ dt,$$

and $\text{erf}(x)$ as the error function.

For example, consider an aluminum target $(k = 226\ \text{W}/(\text{m}\cdot\text{K}), \rho = 2700\ \text{kg/m}^3, c_p = 864.7\ \text{J}/(\text{kg}\cdot\text{K}), \alpha \approx 0.1\ \text{nm}^{-1}$ [36]), an incident laser beam with a peak irradiance I = 100 MW/m^2, and an ambient temperature of $T_0 = 300$ K. The results of a 1D simulation of this engagement are shown in Figure 26.
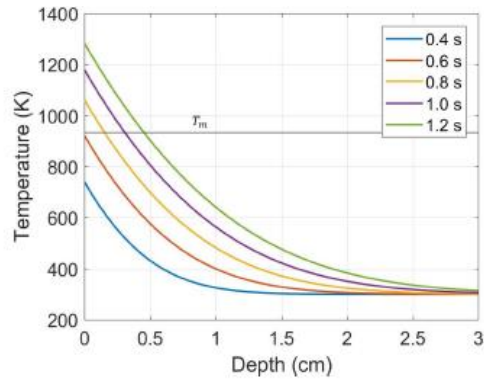
Figure 26. Temperature versus depth for an aluminum target illuminated
by a laser with a peak irradiance of 100 MW/m². Melting
temperature T_m is indicated by the horizontal black line.
Source: [34].

B. MELTING CONSIDERATIONS

Figure 26 shows us the exponential decay of temperature versus depth over time; however, this model does not consider that when the material rises to its melting temperature T_m (933 K for aluminum, for instance) the phase changes and, consequently, the material properties change. This melting process has to be taken into account for realistic modeling.

In the case of a target engaged by a HEL, the irradiance on the target increases the temperature of the (initially solid) material T_s, until it reaches T_m when the change of phase occurs, and the material begins to melt. The HEL continues heating the target, increasing the temperature of the liquid material T_l and melting more of the solid material beneath it; for our simulation, it will be assumed that the liquid material stays in place after it melts, as shown in Figure 27. As a consequence, the phase interface X(t) moves further into the material (downward in the figure).
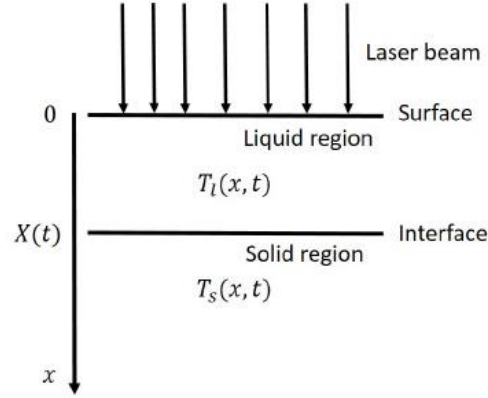
Figure 27. One-dimensional geometrical model of melting due to a laser beam. Source: [34].

In order to incorporate the change of phase into the model, we have to establish an additional boundary condition at the liquid-solid interface $X(t)$. Initially, before irradiation, the temperature of the solid region T_s is equal to the ambient temperature of the air T_0, and the solid-liquid interface location is defined as $X(t = 0) = 0$.

At the liquid-solid boundary, the temperature is equal to the melting temperature of the material T_m ($T_l = T_s = T_m$), and energy is conserved across the boundary such that

$$k_l \frac{\partial T_l(x,t)}{\partial x} = k_s \frac{\partial T_s(x,t)}{\partial x} - \rho L \frac{dX(t)}{dt},$$

where L is the heat of fusion (the amount of heat Q required to melt per unit mass), and Q is the heat added to our system. This formula explains how energy is conserved during a phase transition from liquid to solid: some heat goes into the solid material and the rest of the energy initiates the phase change.

The analytical solutions for each phase (including the interface) considering the previous boundary conditions for a one-dimensional model are as follows [36].

1.   Liquid region ($0 \leq x < X(t)$)

$$T_l(x,t) = T_m - \frac{AI}{k_l}[x - X(t)] + \frac{AI}{2D_l k_l \left[1 + \frac{X(t)}{D_l} \frac{dX(t)}{dt}\right]} \times \frac{dX(t)}{dt}[x^2 - X^2],$$

where A is the absorptivity of the material, and D is the thermal diffusivity of the material.

38

2.   Solid region $(X(t) < x \leq \infty)$

$$T_s(x,t) = T_m - (T_m - T_0)\left\{1 - \exp\left[-\frac{1}{D_s}\frac{dX(t)}{dt}(x - X(t))\right]\right\}.$$

3.   Liquid-solid interface $x = X(t)$

$$X(t) = \left[-\frac{b_0}{2} + \left(\frac{b_0^2}{4} + \frac{a_0^3}{27}\right)^{1/2}\right]^{1/3} + \left[-\frac{b_0}{2} - \left(\frac{b_0^2}{4} + \frac{a_0^3}{27}\right)^{1/2}\right]^{1/3} - \frac{D_l m_s}{16AI},$$

with

$$m_s = \rho\left[c_p(T_m - T_0) + L\right],$$

$$a_0 = \frac{3D_l^2 m_s^2}{256(AI)^2}\left(\frac{192(AI)^2 t}{D_l m_s^2} + 31\right),$$

$$b_0 = -\frac{D_l}{8AI}\left[\frac{D_l^2 m_s^3}{256(AI)^2}\left(\frac{288A^2 I^2 t}{D_l m_s^2} + 47\right) + \frac{t(18A^2 I^2 t + 3D_l m_s^2)}{m_s}\right].$$

Using the same conditions presented in Figure 26, we can plot the temperature versus depth at different dwell times considering the change of phase. In Figure 28, we can observe a kink at the melting temperature due to the phase change, resulting in an abrupt change in the slope of temperature versus depth.
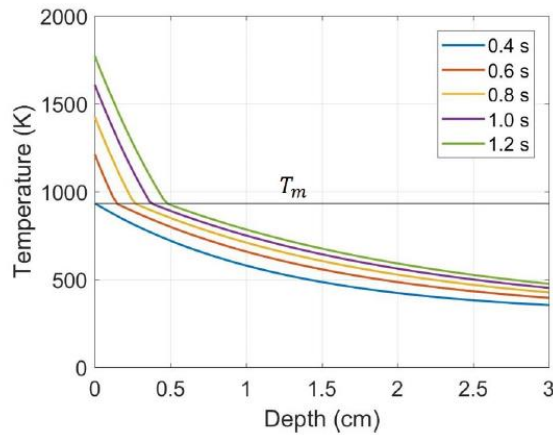
Figure 28.   Temperature versus depth considering melting effects. Melting temperature T_m is indicated by the horizontal black line. Source: [34]

THIS PAGE INTENTIONALLY LEFT BLANK

VI.   MODEL DESCRIPTION

The model for this project will be based on three-simulation codes: the atmospheric extinction coefficients will be provided by the MODTRAN radiative transfer code, the irradiance of the laser onto the target will be provided by the ANCHOR laser performance code, and the resulting effects on the target will be determined using the COMSOL Multiphysics code where we can build a more accurate 3-D model of heat transfer than the 1-D model we discussed in the previous chapter. The results will include graphs of the temperature against the depth in the target for various dwell times using realistic laser output powers.

A.   MODTRAN

Moderate Resolution Transmission (MODTRAN) is a radiative transfer code that models the transmission of electromagnetic radiation across a range of wavelengths through the atmosphere, as shown in Figure 29, taking into account absorption and scattering due to molecules and aerosols. MODTRAN calculates extinction coefficients within finite spectral bands. The atmospheric conditions incorporate a database of transmission spectra for various molecular species: The High-Resolution Transmission (HITRAN) database maintained by the Harvard-Smithsonian Center for Astrophysics. MODTRAN was developed by Spectral Science Inc. and the Air Force Research Laboratory, and it is widely used in the remote sensing community.
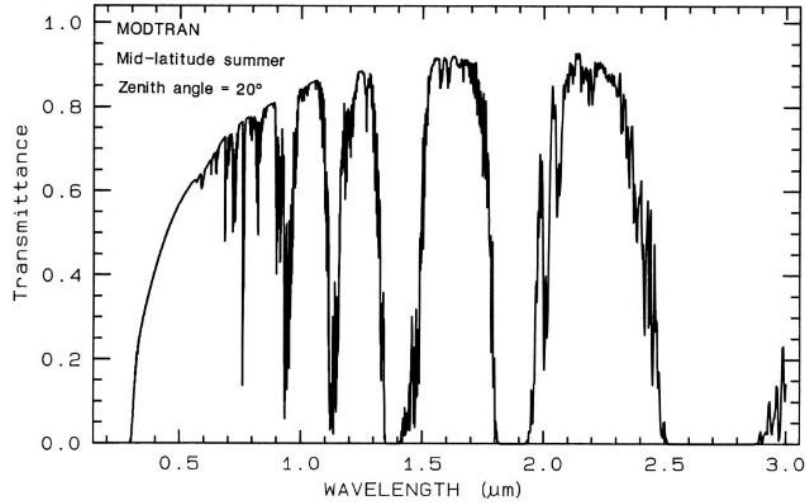
Figure 29. Transmittance (effectiveness in transmitting radiant energy) versus wavelength calculated by from MODTRAN. Source: [37].

MODTRAN has several built-in presets for molecular, aerosol, cloud, and rain models; however, these presets also can be replaced by user-measured values. The preset options for reference atmospheres, as shown in Table 6, determine the temperature, pressure, density, and mixing ratios for H_2O, O_3, CH_4, CO and N_2O. These atmospheres represent various locations in the Northern hemisphere [37].

Table 6. Reference atmospheres for MODTRAN referenced to Northern Hemisphere locations. Source: [37].

MODEL ATMOSPHERE	LONGITUDE	TIME OF THE YEAR
TROPICAL	15 deg. N	ANNUAL AVERAGE
MID-LATITUDE SUMMER	45 deg. N	JULY
MID-LATITUDE WINTER	45 deg. N	JANUARY
SUB-ARTIC SUMMER	60 deg. N	JULY
SUB-ARTIC WINTER	60 deg. N	JANUARY
US STANDARD	NA	1976

The aerosol models in MODTRAN are established for regions that have typical aerosol sources. Those regions are defined as rural, urban, desert, and maritime environments [37]. For high altitudes, the aerosol composition is assumed equal whether

over sea or over land. The aerosol composition also changes between vertical layers of the atmosphere. The modeling of aerosols is provided by two functions:

- The accurate representation of the chemical and physical properties of the aerosol particles, to account for their optical properties, e.g., the complex refractive index.

- The accurate representation of the vertical distribution of the aerosol particle number concentration in the atmosphere.

B.   ANCHOR

ANCHOR is a scaling code developed by the NPS Physics Directed Energy Group which uses inputs from atmospheric codes and databases such as MODTRAN and laser output parameters to estimate the irradiance of the laser beam on the target.

This code, as we will see in the equations below, takes into account the effects caused by diffraction of the light, platform and target jitter, atmospheric extinction, turbulence, and thermal blooming. However, the thermal blooming effect is not considered for our purposes for the reasons explained in Chapter IV.

To calculate the irradiance on the target, ANCHOR uses the following formula [38]

$$\langle I \rangle = \left(\frac{P e^{-\int \epsilon(z) dz}}{\pi w_{tot}^2} \right) S_{TB},$$

where $\langle I \rangle$ is the irradiance onto the target averaged over time, P is the laser output power, $\epsilon(z)$ defines the coefficient of extinction along the beam path, S_{TB} represents the thermal blooming Strehl ratio, and w_{tot}^2 is the spot size at the target. As mention before, thermal blooming will not be taken into account for this simulation, so we will assume $S_{TB} = 1$.

The spot size at the target is defined as [38]

$$w_{tot}^2 = w_d^2 + w_j^2 + w_t^2,$$

43

where w_d is the diffraction contribution, w_j is the jitter contribution, and w_t is the turbulence contribution. Those contributions are calculated using the equations [38]

$$w_d = M^2 \left(\frac{2\lambda R}{\pi D} \right),$$

$$w_j = \theta_{RMS} R,$$

$$w_t = \frac{2\lambda R}{\pi r_0},$$

where M^2 is the quality factor of the laser beam (>1 for non-ideal), R is the range of the target, D is the diameter of the laser beam at the beam director, λ is the wavelength of the laser beam, θ_{RMS} is the angular variance due to jitter, and r_0 is the Fried parameter (diameter over which the beam maintains transverse coherence throughout the propagation length). For the case of constant refraction structure parameter, C_n^2 (see Section 2 of Chapter IV), the Fried parameter for a focused beam is calculated as

$$r_0 = 0.33 \left(\frac{\lambda^{6/5}}{R^{3/5}(C_n^2)^{3/5}} \right).$$

For simulation purposes, we will use the Hufnagel-Valley 5/7 (HV 5/7) turbulence profile explained in Chapter IV.

C.   COMSOL MULTIPHYSICS

COMSOL Multiphysics is a simulation platform created by the COMSOL Group company in July 1986 in Stockholm, Sweden. It is used by scientists and engineers from many research fields to model and analyze the behavior of particular systems, incorporating many physical effects including mechanics, electromagnetism, heat transfer, and fluid flow. Various steps are required for the COMSOL modeling process, as we will show in the following sections, including: defining the geometry; specifying material properties, boundary conditions, and the physics equations to be used; setting up the mesh; and running the simulation. The user can decide how COMSOL presents the results, including 2-D or 3-D graphs, animations, etc.

COMSOL Multiphysics consists of various different modules such as a heat transfer module, an electromagnetism module, an acoustic module, etc., each of them with their own capabilities to model particular aspects of a system. For our purposes we will use the heat transfer module to study how heat flows into a target, and to study how much of the target is melted as it irradiated by a laser.

1. Defining Geometry

After creating a new component, the first step is to build the geometry from the model builder specifying its dimensions and orientations. There are various geometries that could be selected; COMSOL also allows the user to import geometries from other programs. Figure 30 shows a cylinder geometry of 5 cm radius and 5 cm thickness from the model builder.
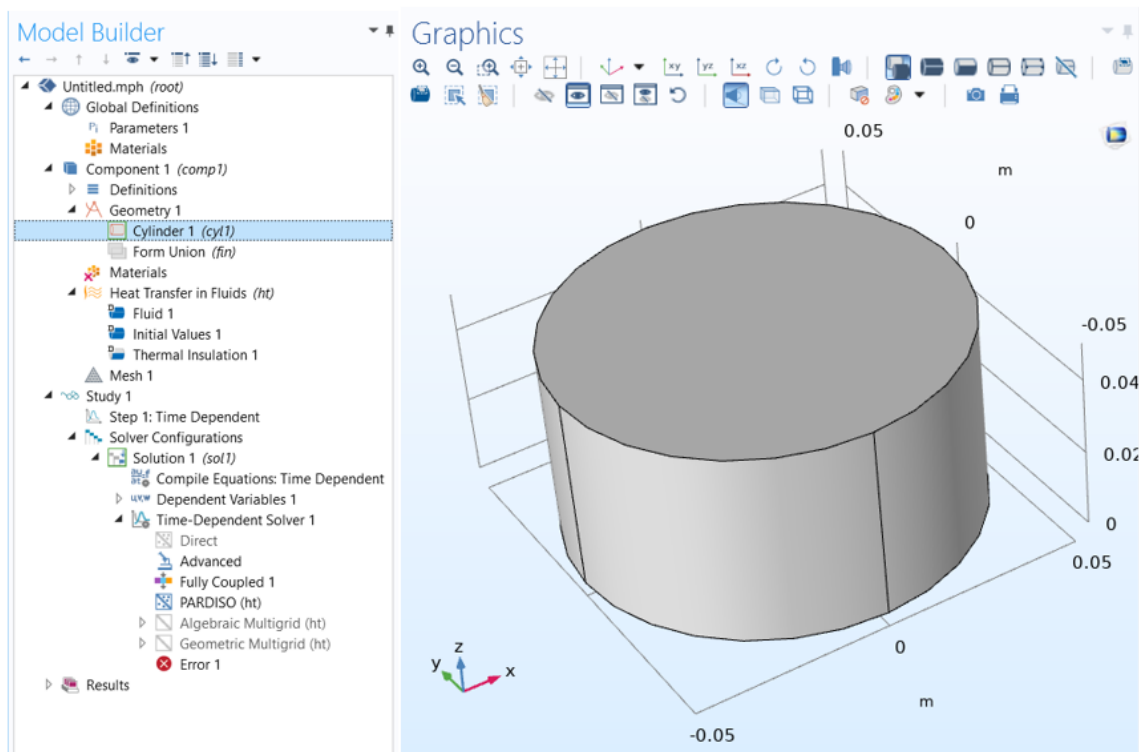
Figure 30.   Cylinder geometry of 5 cm radius and 5 cm thickness from the model builder.

2. Specifying Material Properties

The next step is to define the material that our target will be made of; to do so, COMSOL has an extensive library of materials. This library depends on which module of COMSOL is in use. Figure 31 shows the aluminum material selection from the model builder.
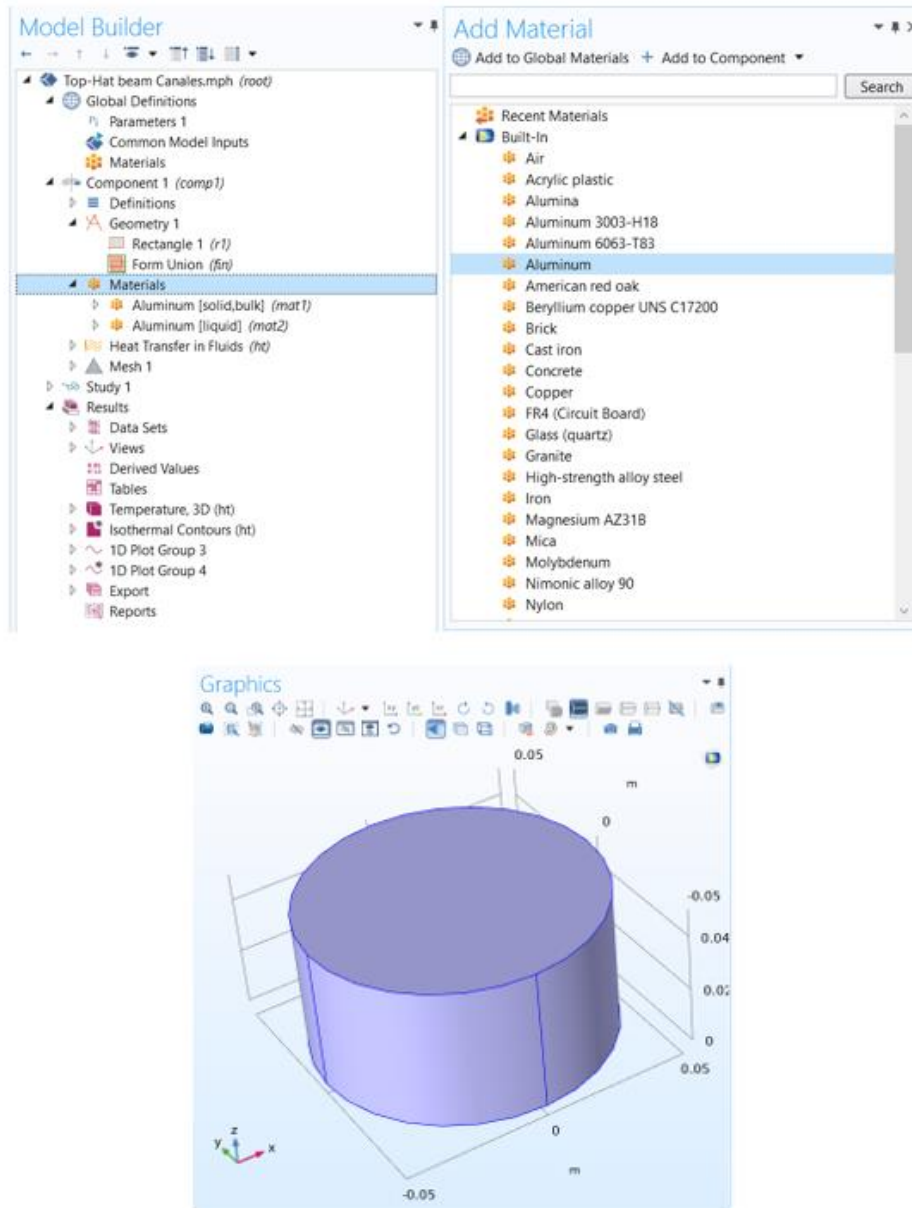
Figure 31.   Aluminum material selection from the model builder.

3. Boundary Conditions

Then it is necessary to specify the boundary conditions. As Figure 32 shows, we selected the top region to deposit the laser beam energy. We also selected the top, sides and below region as thermal insulators to not allow heat to flow beyond those regions.
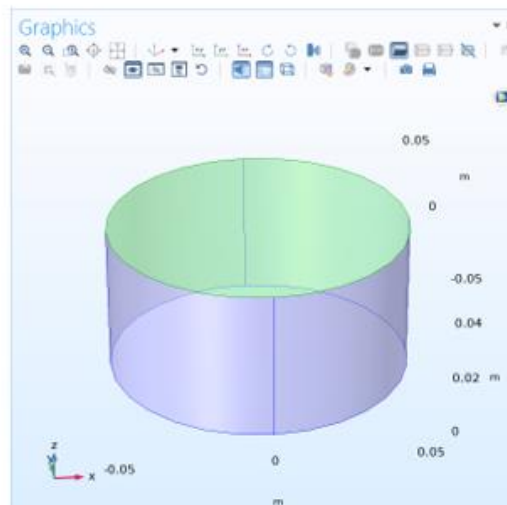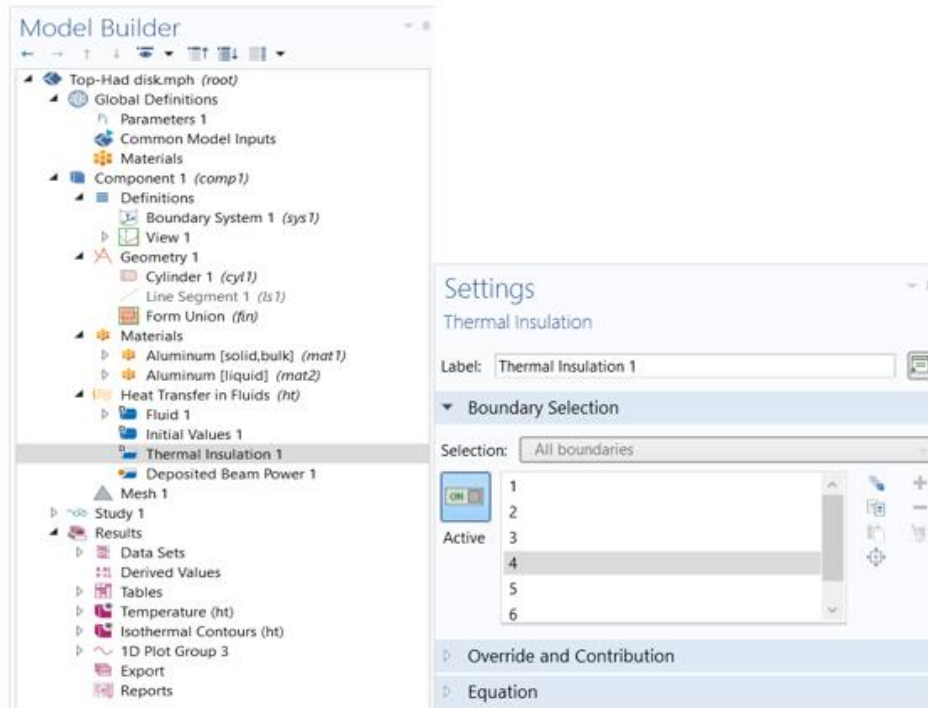
Figure 32.   Boundary conditions selection.

4. Specifying the Physics Equations to be Used

This step is where we tell COMSOL what to do with our material; i.e., what will happen to our target under some physical conditions. COMSOL is already equipped with a library of equations for each physics phenomena; however, we can modify those equations as needed. Numerical values are required to fill out the equations. As with the materials library, the physics section depends on the COMSOL module in use. Figure 33 shows how we build a model for heat transfer from a laser beam with a uniform intensity of 100 MW/m^2 and a spot size radius of 12 mm hitting our aluminum cylinder (5 cm radius and 5 cm thick). For the thermal properties of aluminum, its melting point is set at 933 K, the latent heat of fusion is 397 kJ/kg, and the rest of the parameters (thermal conductivity, density, etc.) are taken from the materials library.
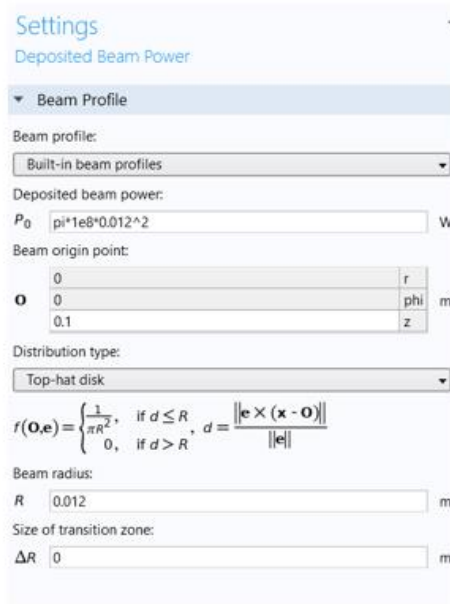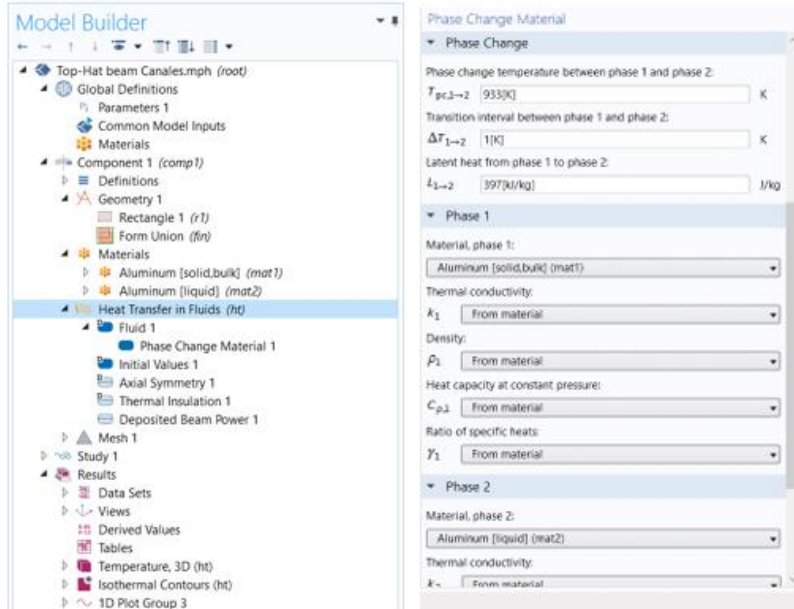
Figure 33.   Heat transfer physics selection for a laser beam of irradiance
100 MW/m^2 and spot size radius of 12 mm hitting an aluminum
cylinder of 5 cm radius and 5 cm thickness considering a
change of phase at 933 K and a latent heat from solid to liquid
aluminum of 397 kJ/kg.

5.   Results

Finally, we compute the model to get a numerical temperature profile as a function of time. We can plot this information in any number of ways; for example, Figure 34 shows a 3-D cross-section of the temperature profile of the aluminum target after 80 seconds of illumination.
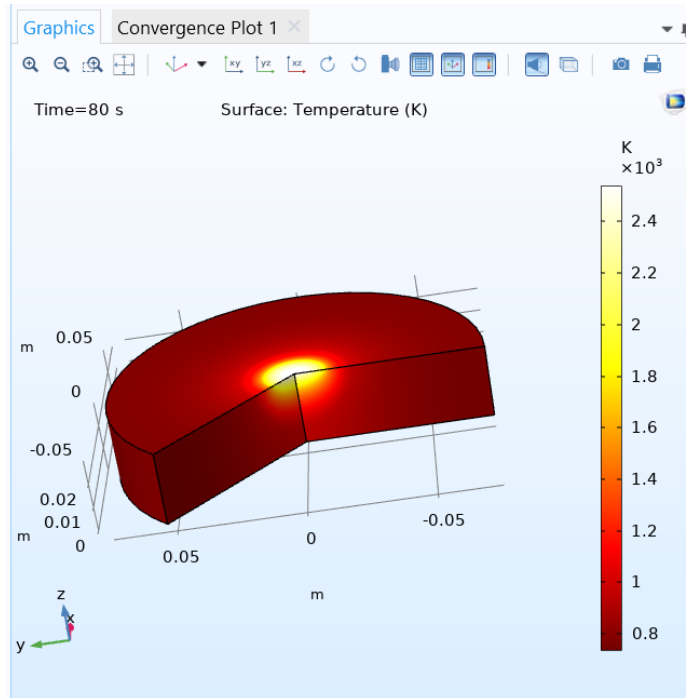
Figure 34.   3-D presentation of laser beam of irradiance 100 MW/m^2 and spot size radius of 12 mm hitting an aluminum cylinder of 5 cm radius and 5 cm thickness.

D.   COMSOL MODEL VALIDATION

An analytical 1-dimensional treatment of target melting was discussed in Carlos Romero's thesis [34]; that 1-D model was built with MATLAB (see Figure 35). A summary of this 1-D model is given in Chapter V.

Romero's model assumes a semi-infinite 1-D geometry with aluminum properties for the target irradiated by a 100 MW/m^2 peak irradiance; it includes the effect of phase change from a solid to a liquid as discussed in previous chapters.
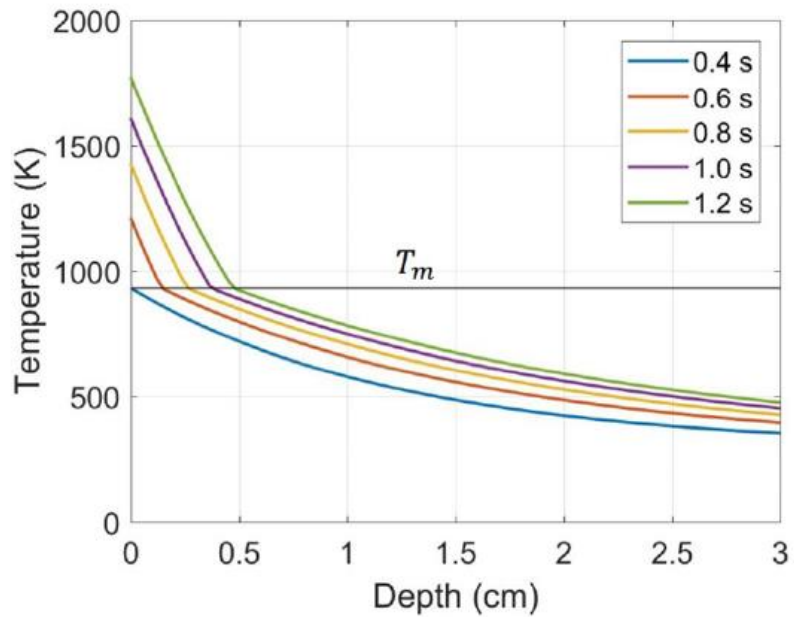
Figure 35.   Temperature versus depth at different dwell times from
MATLAB Romero's results for a 1-D semi-infinite target
geometry irradiated by a 100 MW/m^2 laser beam.

Our model, on the other hand, uses a 3-D aluminum cylinder geometry with a radius of 5 cm and a depth of 5 cm irradiated by a 100 MW/m^2 peak irradiance beam with a spot size of the same radius of the cylinder (5 cm), as we can see in Figure 36. The plot includes melting effects as well. Results are show in Figure 37. By making the spot size the same as the target radius (and specifying insulating boundary conditions), our 3-D COMSOL model approximates 1-D behavior; therefore, we can compare its directly to the analytical model described in Romero's thesis.
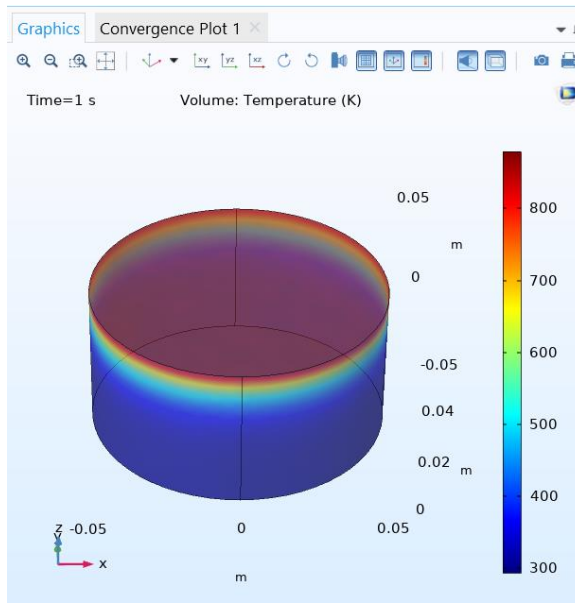
Figure 36.   Aluminum cylinder geometry with a radius of 5 cm and a depth
of 5 cm irradiated by a 100 MW/m^2 peak irradiance beam with
a spot size of the same radius of the cylinder (5 cm)
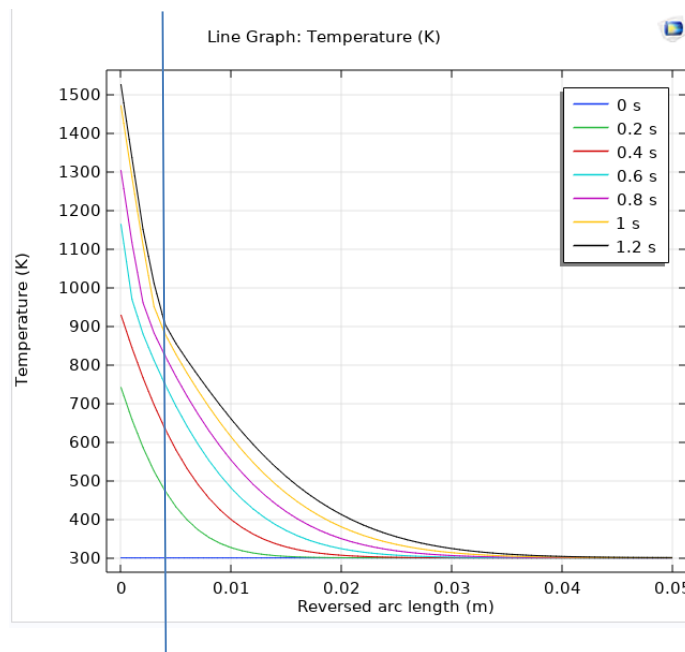
Figure 37.   Temperature versus depth at different dwell times from
COMSOL results for a 3-D aluminum cylinder target geometry
irradiated by a 100 MW/m^2. The vertical line shows position of
the change of phase after 1.2 seconds.

The melt depth in this model is shown by the phase change, in Figure 37 this effect is shown by a kink in the plot lines.

We can observe two relevant differences between the plots:

- Slightly lower temperatures predicted on the surface from the 3-D COMSOL model after 1.2 seconds of illumination.

- Slightly less melt depth after 1.2 seconds predicted by the COMSOL model, (around 0.4 cm) in comparison to the 1-D analytic result (0.5 cm).

The results from both models are in otherwise good agreement.

In a more realistic case where the spot size is much less than the target, heat will diffuse in a three-dimensional manner into the surrounding material. We expect the melt depths to be greatly reduced due to this effect than a simpler 1-D model would predict.

E. INTEGRATED DIAGRAM

The diagram presented in Figure 38 illustrates the procedural flow of our simulation with its inputs and outputs from: external data (dark purple) and its codes (blue); and its results (green), where the Hufnagel-Valley 5/7 model and MODTRAN provide the atmospheric parameters for turbulence and extinction respectively; the ANCHOR model is fed by those atmospheric parameters and laser parameters, including beam director size and laser power. ANCHOR provides two outputs: peak irradiance and spot size of the laser beam at the target. Those outputs are used by COMSOL together with the target material properties to model heat flow and finally obtain a result represented by a plot of temperature versus melt depth for different dwell times.
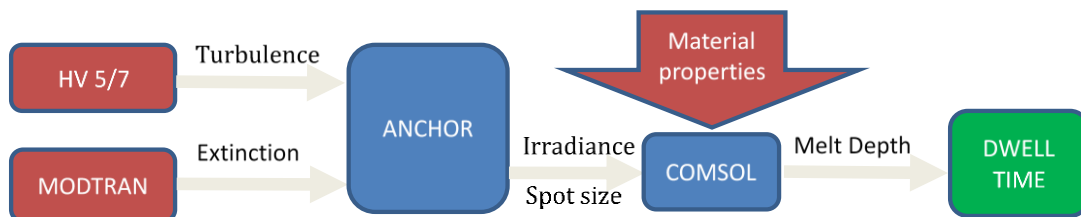
Figure 38.   Simulation research integrated diagram.

THIS PAGE INTENTIONALLY LEFT BLANK

VII. SCENARIOS AND PARAMETERS

In this simulation, we will try to engage a small watercraft transporting a huge amount of cocaine that is trying to pass over the 200-mile limit to international waters. The maximum speed of the boat is 35 knots. Our goal will be to stop it by disabling the engine from a laser based on a UAV with no collateral damage to cargo and/or personnel on board. To do so, we need to select a HEL from Chapter II consistent with our previously discussed scenario. Later, we will estimate the total weight of the laser system, including the laser components (gain medium and cavity), the beam director, the thermal management system (cooling), and the power supply system (batteries). On the basis of those results we can establish the most suitable UAV platform from Chapter III. Finally, we will establish the target parameters and the atmospheric conditions for our engagement.

A. HIGH ENERGY LASER

From the discussion in Chapter II, it was established that a solid-state fiber laser is the best option for our purposes. It is more compact at the same power output compared with the other lasers, its magazine is limited only by available electrical energy, and it has favorable characteristics for propagation in maritime environments. Our solid-state laser will have the following properties: an output power of 10 kW, 25 kW, or 50 kW with a uniform beam shape, a beam quality $M^2 = 1.5$, an angular variance due to jitter $\theta_{RMS} = 5$ µrad [37], a beam director diameter of 20 cm, and a wavelength $\lambda = 1.064$ µm.

B. ENERGY STORAGE CAPACITY

In this simulation, we will consider 15 min as the maximum time that the solid state laser can operate, for one or several engagements. The corresponding energy storage needed will be calculated from the following equation

$$E_S = \frac{Pt}{\eta},$$

where E_S is the energy storage capacity in joules (J), P is the laser output power in watts (W), t is the maximum lase time in seconds (s), and η is the laser efficiency (assumed to

be 0.25). Thus, for a 25 kW laser operating for 15 minutes, we require this much energy storage

$$E_S = \frac{(25 \times 10^3 \text{ W}) \ (900 \text{ s})}{0.25} = 90 \text{ MJ}.$$

With the required energy storage established, we have to calculate the weight of the batteries needed to store that amount of energy; it will be calculated from the equation

$$E_S = SE \times W_{ES} \times 3600 \text{ s/h},$$

where E_S is the energy storage, SE is the specific energy of the battery in watt hours per kilogram (Wh/kg), and W_{ES} is the energy storage mass in kilogram (kg).

Rearranging the equation to get the weight of the energy storage yields

$$W_{ES} = \frac{E_S}{SE \times 3600 \text{ s/h}}.$$

For this estimate, lithium-ion batteries will be used. Table 5 provides the specific energy of Li-Ion batteries: $SE \sim$ 120-160 Wh/kg. Thus,

$$W_{ES} = \frac{90 \times 10^6 \text{ Ws}}{120 \frac{\text{Wh}}{\text{kg}} \times 3600 \frac{\text{s}}{\text{h}}} \approx 210 \text{ kg}.$$

C.   TOTAL SYSTEM WEIGHT

The total system weight for a HEL weapon can be calculated from the equation

$$W_{TOT} = W_{BD} + W_L + W_{ES} + W_{TH},$$

where W_{TOT} is the total weight, W_{BD} is the beam director weight, W_L is the laser weight, W_{ES} is the power supply weight, and the W_{TH} is the thermal management system weight.

Each of the terms in this equation, except W_{BD}, will scale approximately linearly with the laser output power; W_{ES} and W_{TH} will also depend on the laser efficiency. Also, as described in the previous section, W_{ES} will depend on the maximum laser operating time.

The weight of a typical beam director, for instance the MZA Othela (which has a 30 cm aperture), is $W_{BD} \sim 225$ kg [42]. The weight of the laser system itself can be estimated using 5 kg/kW [43]; i.e., for a 25 kW laser, $W_L \sim 125$ kg. The weight of the energy storage system was discussed in the previous section. The weight of the thermal management system, for a 25 kW laser with 25% efficiency, can be estimated as $W_{TH} \sim 750$ kg [40]. Thus, for this example, the total system weight would be

$$W_{TOT} \sim 225 \text{ kg} + 125 \text{ kg} + 210 \text{ kg} + 750 \text{ kg} = 1310 \text{ kg}.$$

D.   PLATFORM

The UAV we will consider will be a MQ-4C Triton, discussed in Chapter III, operating at various altitudes from 500 m to 10 km. The maximum payload of this platform is 1452 kg so from the previous calculation it could carry our 25 kW laser. Nowadays, there are a few UAVs that have a payload capacity greater than 2500 kg, such as the Heron TP (payload capacity $\sim$ 2700 kg) and the Predator C Avenger (payload capacity $\sim$ 2948 kg) [41], so these platforms may be able to carry a larger 50 kW laser.

Figure 39.   Drug trafficking watercraft captured in Ecuador with more than $28 million worth of cocaine onboard. Source: [38].

E.   TARGET

A typical drug trafficking watercraft is presented in Figure 39. Its main characteristic, or at least the most important for our purposes, is the three outboard motors. These motors represent a vulnerable area of the craft and make attractive targets for a laser weapon. Most outboard motor materials are aluminum with a fiberglass polyester resin composite dome cover on the top. The fiberglass dome is only about 2 mm thick and will otherwise be ignored for estimating dwell times. The bulk aluminum in the motor is about 3 cm thick [33]. Table 7 shows some important aluminum parameters.

Table 7.   Target material parameters. Adapted from: [33].

Parameter	Material
	Aluminum
Density (ρ) [kg/m^3]	2700
Melt Temperature (T_m) [K]	933
Latent Heat of fusion (L) [J/Kg]	3.97x10^5
Thermal conductivity in solid state (k_s) [W/m·K]	226
Thermal conductivity in liquid state (k_l) [W/m·K]	92
Operation Temperature (T_0) [K]	360
Absorptivity (A)	0.202
Thickness [cm]	3

F.   ATMOSPHERIC CONDITIONS

The atmosphere parameters will be taken from a MODTRAN model, with these specifications: tropical environment, 23 km of visibility, and maritime aerosol profile. We will assume a sea level temperature of 300 K.

THIS PAGE INTENTIONALLY LEFT BLANK

VIII. MODEL RESULTS

By running the ANCHOR code with the specifications described in Chapter VIII, we obtain two plots: a peak irradiance plot and a spot size plot, both versus cross range to the target for various UAV platform heights. Those values are needed to establish the most effective tactics for the engagement from our UAV, such as desirable platform heights and ranges, and then to calculate the required dwell times for target damage using the COMSOL model.

A.   SPOT SIZE VERSUS CROSS RANGE

As mentioned in the previous chapter, the spot size is a turbulence-dependent variable that indicates the radius of the laser beam on the target. The spot size does not depend on the output power for our case since we are ignoring thermal blooming. Figure 40 shows the plot for the spot size versus cross range for various platform heights.
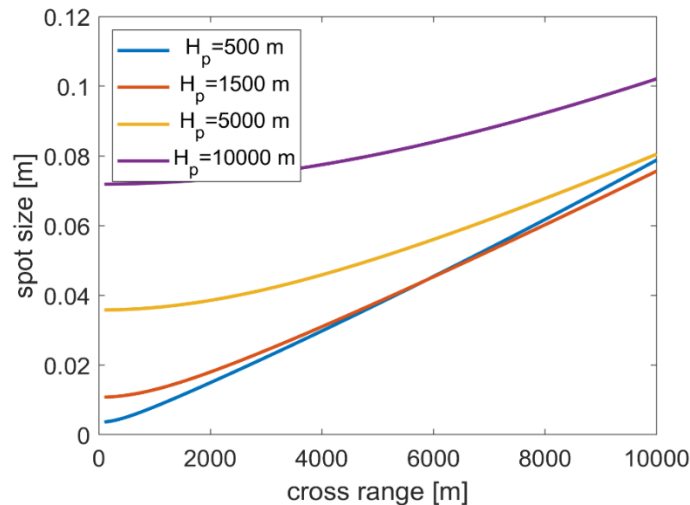
Figure 40.   ANCHOR results for spot size versus cross range from the target for various platform altitudes.

The general trend is that the spot size increases with height and cross range due to the beam traveling more distance through the atmosphere. Furthermore, since turbulence

is greater at low altitudes (see chapter IV), we can observe an intersection point for the $H_p = 500$ m and 1500 m curves at a cross range about 5000 m; beyond that, it is slightly better to be at the higher altitude—even though the beam has to travel through a greater distance, it is through a region of lower turbulence (on average).

B. PEAK INTENSITY VERSUS CROSS RANGE

The peak intensity is the amount of power per unit area that reaches the target at its peak value (i.e., in the center of the beam for a Gaussian profile). It is important to note that the peak intensity is not only turbulence-dependent but extinction-dependent as well. The peak intensity, unlike the spot size, does depend on the output power of the source, so in the following graphs it will be presented for various output power values. Figures 41, 42, and 43 plot the peak intensity versus cross range for 10 kW, 25 kW, and 50 kW laser output power, for various platform heights. Even though the laser power selected in the previous chapter was 25 kW to fit within the payload capacity of the MQ-4C Triton, we show these other output powers to analyze a broader spectrum of capabilities.
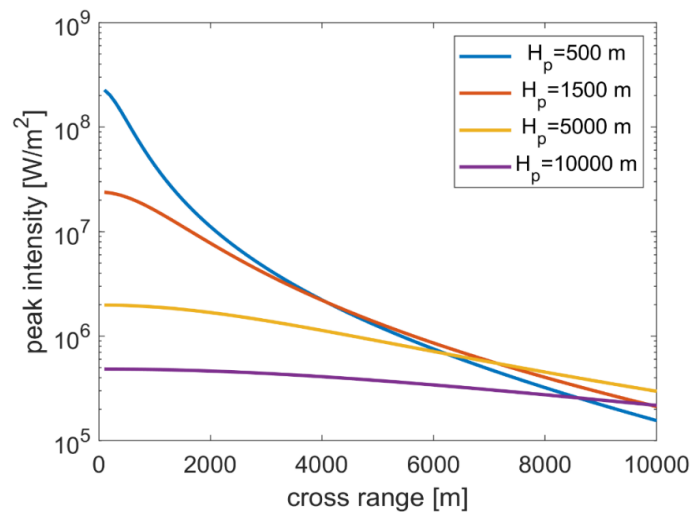
Figure 41. ANCHOR results for peak intensity versus cross range from the target for various platform altitudes for a 10kW output power laser.
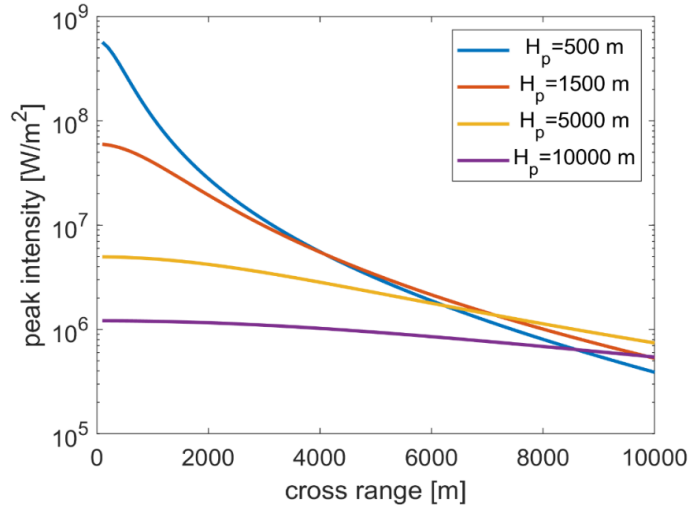
Figure 42.   ANCHOR results for peak intensity versus cross range from the target for various platform altitudes for a 25kW output power laser.
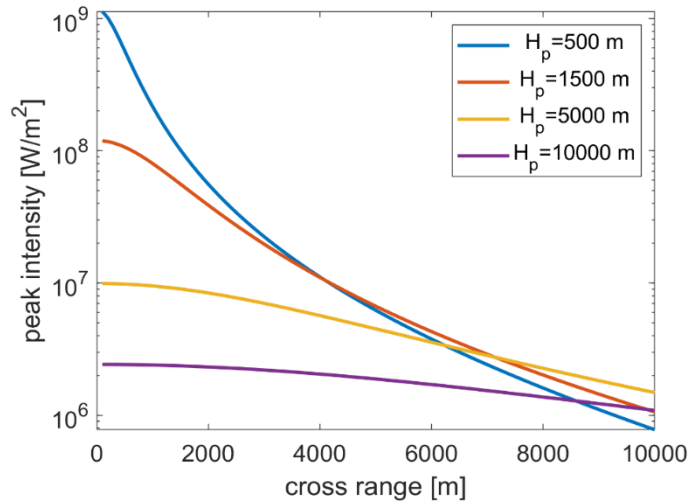
Figure 43.   ANCHOR results for peak intensity versus cross range from the target for various platform altitudes for a 50kW output power laser.

As we can observe, the shapes of the plots are the same because the atmospheric conditions do not change; however, the magnitude of the peak intensity (the vertical axis) increases with laser output power. Another important result is that the peak intensity decreases more rapidly versus cross range at the lowest altitudes; this is due to the laser

beam having to pass through more of the region of high extinction and turbulence. For example, we can observe that for a 25 kW laser at 500 m (the blue curve in Figure 42), the laser beam will have a peak intensity of approximately $4 \times 10^8 \text{W/m}^2$ if it is emitted directly above the target, whereas it will have a peak intensity of around $3 \times 10^5 \text{ W/m}^2$ if it is emitted at a cross range of 10 km from the target.

C.   TACTICS OF THE ENGAGEMENT

In light of these results, to avoid the significant decrease of peak intensity at long cross ranges and high-altitude engagements, we will consider cross range of 500 m, 1 km, and 2 km range away from the target, and platform heights up to 1500 km.

D.   DWELL TIME

Tables 8, 9, and 10 show the plots of temperature in kelvin versus melt depth in meters obtained from the COMSOL model for a 10 kW, 25 kW, and 50 kW power laser at 500 m and 1500 m height, and at 500 m, 1000 m, and 2000 m of cross range. The melt temperature for aluminum is represented by the horizontal black line in our plots. The various colored curves correspond to different dwell times, as indicated by the legend. Thus, the required dwell time to melt through 3 cm of aluminum can be determined from these plots by observing which colored line intersects the black line on the far right side of the plot. For instance, consider the upper left plot in Table 9 (25 kW laser, 500 m height, 500 m cross range); for that case, the black line intersects the red curve at $r = 0.03$ m, so according to the legend it would take the laser approximately 180 s to melt through 3 cm of aluminum from that range and altitude.

It is important to note in our COMSOL modeling we are not considering vaporization of aluminum (a second change of phase) so the plots that exceed the temperature of 2750 K (boiling temperature of aluminum) will not be considered for our conclusions.

Table 8.   10 kW laser output plots of temperature (K) versus melt depth (m)
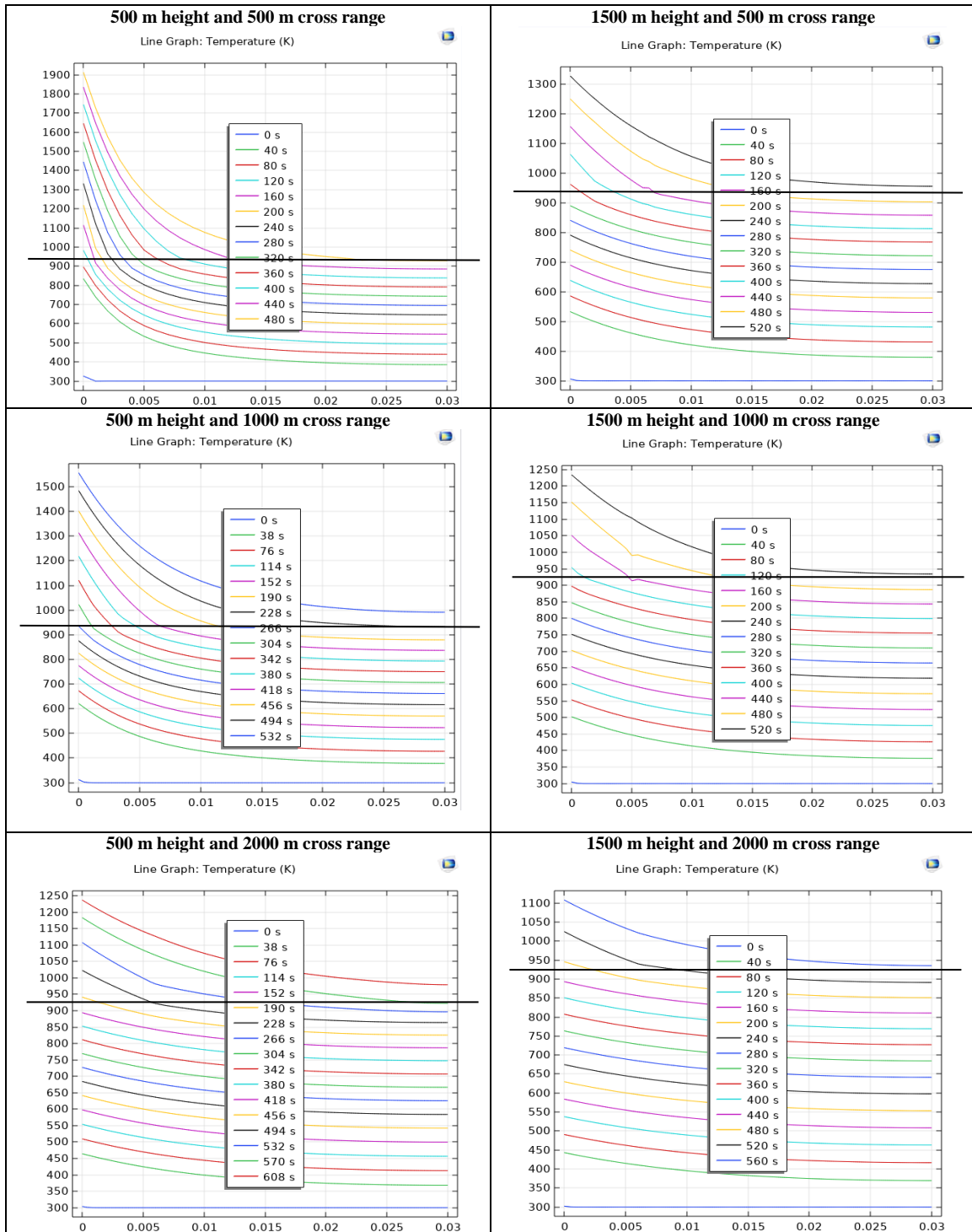at different ranges and heights.

Table 9.   25 kW laser output plots of temperature (K) versus melt depth (m)
at different ranges and height.
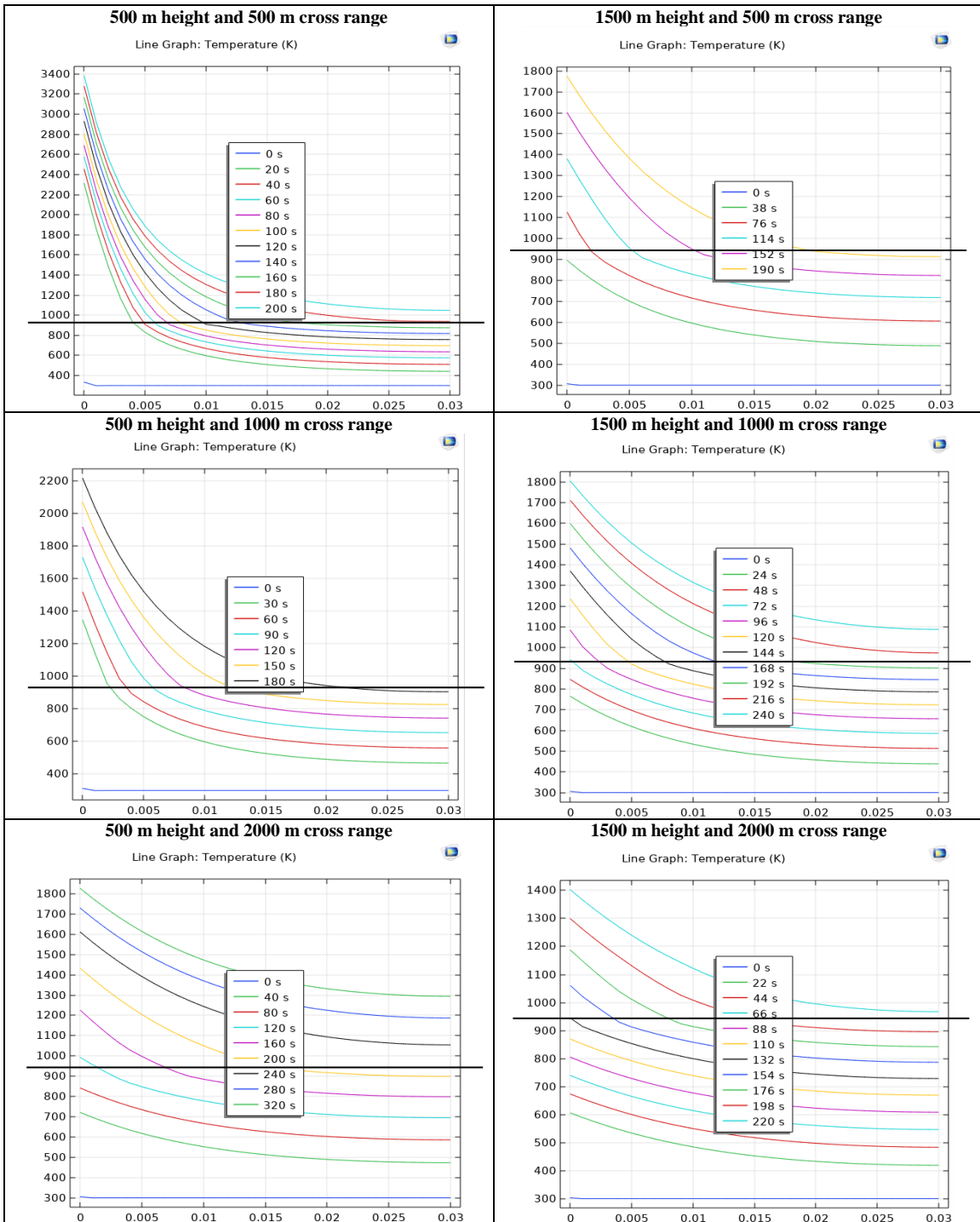
Table 10.   50 kW laser output plots of temperature (K) versus melt depth (m)
at different ranges and height.
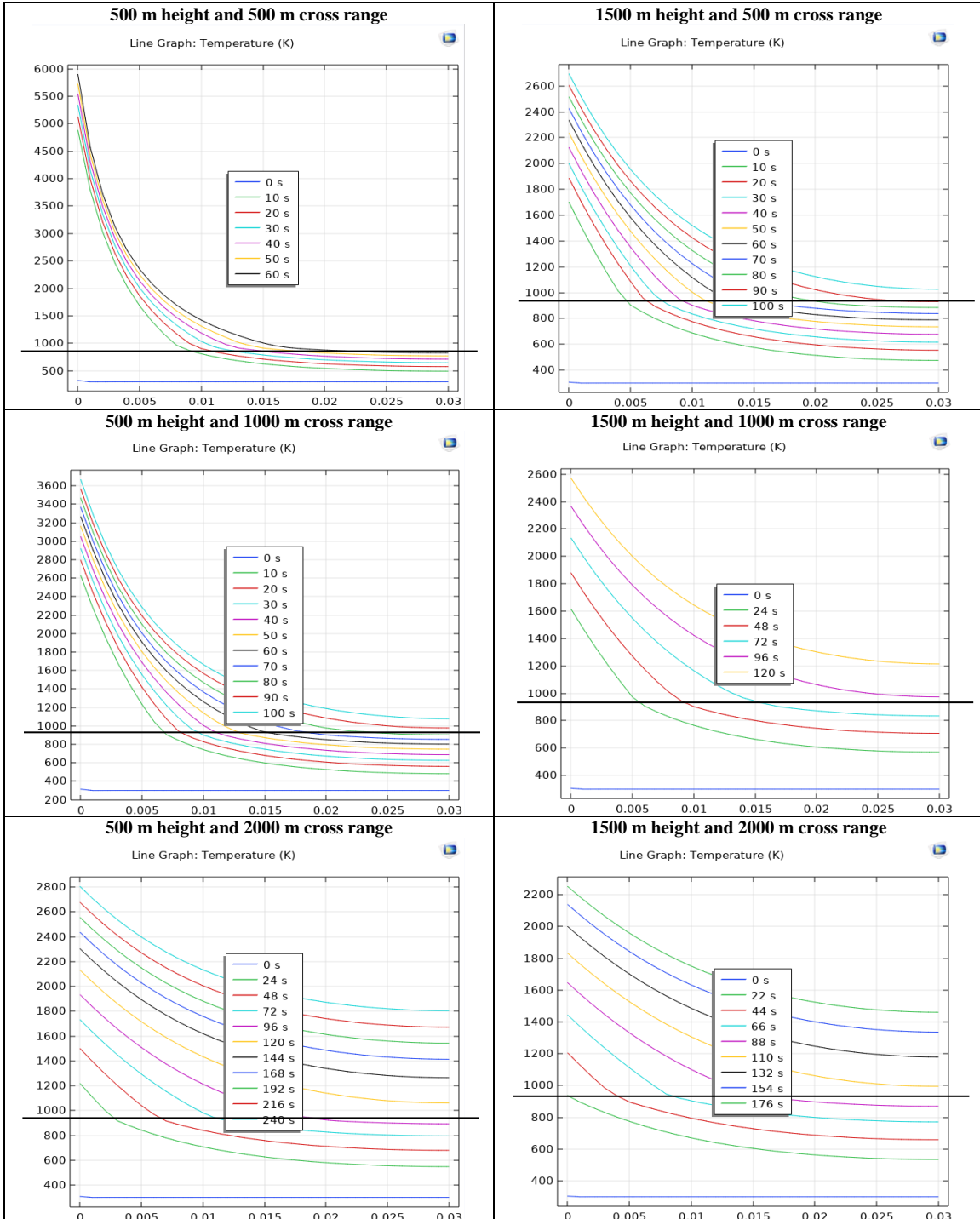
Table 11 shows a summary of the previous tables and shows the dwell times at different laser powers, ranges, and heights.

Table 11.   Dwell times for 10 kW, 25 kW, and 50 kW power laser at different ranges and heights

10 kW power laser			
Height/ Range	500 m	1000 m	2000 m
500 m	480 s	495 s	570 s
1500 m	505 s	510 s	550 s
25 kW power laser			
Height/ Range	500 m	1000 m	2000 m
500 m	NA	180 s	210 s
1500 m	190 s	205 s	215 s
50 kW power laser			
Height/ Range	500 m	1000 m	2000 m
500 m	NA	NA	100 s
1500 m	90 s	88 s	92 s

From Table 11 we can see that for a given laser output power, the dwell time does not vary much with platform height and range, so we can establish an average dwell time for each laser output power:

- 10 kW ~ 8 – 9 minutes.

- 25 kW ~ 3 – 3.5 minutes.

- 50 kW ~ 1.5 minutes.

As expected, a greater laser output power results in a shorter dwell time; i.e., less time to disable an engine. Note that these are all quite long dwell times; however, they are all within the capacity that we assumed for our energy storage system (total lasing time of 15 minutes). Also, the small boat target would take more than a few minutes to reach the larger supply ship outside Peruvian maritime domain, and the UAV platform should be able to keep up with and track the boat for an extended time, and continuously apply laser energy on the target. We also have to consider that our model is limited because it does not account for the evaporation of the aluminum and also assumes that the liquid aluminum remains in place. This means that in this model, the heat from the laser must pass through

the liquid layer before reaching the solid layer, and some of the heat also gets absorbed by the liquid. The net result is that this model will overestimate dwell times.

Furthermore, our COMSOL model assumes the melted aluminum pools in place. In reality, the melted aluminum would flow (due to, e.g., gravity), exposing solid aluminum to the laser beam. This will reduce dwell times, so the times presented here should be considered conservative estimates.

Other vulnerable areas of the fast boats that can be potentially hit by a HEL beam, such as the fuel supply lines (5 mm of rubber [34]), were not considered. However, we can presume that such "softer" targets would require much less dwell time than aluminum, considering the materials parameters and the thickness of the targets

THIS PAGE INTENTIONALLY LEFT BLANK.

IX. CONCLUSIONS

The interdiction of fast boats from a UAV equipped with a high energy laser is feasible as long as the platform can carry a payload of about 1300 kg (for a 25 kW laser).

The engagement time required to disable a fast boat will depend on the laser output power mainly; it has a much weaker dependence on range and height (as long as both are within 1500 m). Our results show that for a 10 kW laser, a dwell time of more than 8 minutes is needed, whereas for a 25 kW laser, a dwell time of more than 3 minutes is needed. More powerful lasers would significantly reduce the dwell time, as the 50 kW laser required a dwell time of about 1.5 minutes, but that may increase the payload beyond the capacity of current UAVs. Improvements in laser or battery technology could enable more powerful lasers to fit on UAVs.

Targeting other vulnerable areas such as fuel supply lines will reduce the engagement time, but this was not considered due to limitations in our COMSOL model, so this is an area of potential future research. The model could also be improved to include a second phase change (vaporization) which could lead to more optimistic results, even for aluminum targets.

THIS PAGE INTENTIONALLY LEFT BLANK

LIST OF REFERENCES

[1]   Sociedad Peruana de Derecho Ambiental (SPDA) Actualidad Ambiental
        [Peruvian Society of Ambiental Rights (SPDA) Ambiental Actuality], "Conoce
        los datos más resaltantes de la pesca en el mar Perú art" [Knowing the most
        relevant data about the fishing in the Peruvian Sea], Sep. 14, 2017. [Online].
        Available: https://www.actualidadambiental.pe/?p=46340

[2]   OCEANA Protegiendo a los océanos del mundo [OCEANA Protecting the oceans
        of the world], "La pesca ilegal, un crimen millonario en el mundo art" [The illegal
        fishing, a millionaire crime around the world], Feb. 09, 2016. [Online]. Available:
        https://peru.oceana.org/es/blog/la-pesca-ilegal-un-crimen-millonario-en-altamar

[3]   Felipe Souza and Ricardo Senra, "Un triángulo de drogas, armas y violencia: la
        BBC revela la terrible realidad de la triple frontera entre Brasil, Colombia y Perú"
        [A triangle of drugs, guns, and violence: BBC reveals the terrible reality of the
        triple border between Brasil, Colombia, and Peru], *BBC Brasil*, Mar. 06, 2017.
        [Online]. Available: https://www.bbc.com/mundo/noticias-america-latina-
        39178889

[4]   Ana Briceño, "¿Qué vía usan los narcos para enviar droga al extranjero?" [What
        way does the drug dealer use to send drugs overseas?], *El Comercio*, dic. 13,
        2017. [Online]. Available: https://elcomercio.pe/lima/sucesos/via-narcos-enviar-
        droga-extranjero-noticia-480809

[5]   Constitucion Politica del Peru [Political Constitution of Peru], Art. 165, 1993.
        [Online]. Available: https://www.oas.org/juridico/spanish/per_res17.pdf

[6]   Ley Orgánica de la Marina de Guerra del Perú [Peruvian Navy Organic Law],
        Pub. L. No. 438, Art. 4 (c), 2012. [Online]. Available:
        http://www4.congreso.gob.pe/historico/cip/materiales/meducacion /DL438.pdf

[7]   Ley de creación del cuerpo de capitanías y guardacostas [Creation of the Coast
        Guard branch Law], Pub. L. No. 17824, 2013. [Online]. Available:
        https://www.dicapi.mil.pe/sites/default/files/descargas/normas-
        generales/decreto_ley_ndeg_17824.pdf

[8]   Allied Maritime Interdiction Operations, ATP-71, Brussels, Belgium, 2013.

[9]   G. P. Perram, S. J. Cusumano, R. L. Hengehold, and S. T. Fiorino, *An
        Introduction to Laser Weapon Systems.* New Mexico, USA: The Directed
        Energy Professional Society, 2010.

[10]   "Advantages of DE Weapons," class notes for Directed Energy Weapons: Overview, Dept. of Physics, Naval Postgraduate School, Monterey, CA, USA, fall 2018.

[11]   "Light-Matter Interaction," class notes for Lasers Course, Dept. of Physics, Naval Postgraduate School, Monterey, CA, USA, fall 2018.

[12]   Jeff Hecht, "History of gas lasers, part 1—continuous wave gas lasers," *OSA The Optical Society*, January. 2010. [Online]. Available: https://www.osaopn.org/home/articles/volume_21/issue_1/features/history_of_gas _lasers,_part_1%E2%80%94continuous_wave_gas/

[13]   Glen P. Perram, "Chemical lasers," *Air Force Institute of Technology*. [Online]. Available: http://www.afit.edu/Docs/Chemical%20LasersWeb.pdf

[14]   "Fiber Laser Systems," *Photomachining*. [Online]. Available: https://www.photomachining.com/laser-micromachining-products-fiber/

[15]   Talal Husseini, "HEL on high water: The top Navy laser weapon systems," Naval Technology, Apr. 01, 2010. [Online]. Available: https://www.naval-technology.com/features/navy-laser-weapon-systems/

[16]   Congressional Research Service, "Navy Lasers, Railgun, and Gun-Launched Guided Projectile: Background and Issues for Congress," Washington, DC, USA, Rep. R44175, 2019. [Online]. Available: https://fas.org/sgp/crs/weapons/R44175.pdf

[17]   Slide from February 2016 ONR briefing to CRS on SSL-TM program, received from Navy Office of Legislative Affairs February 26, 2016.

[18]   P. Fahlstrom and T. Gleason, *Introduction to UAV Systems*, 4th ed. The Atrium, Southern Gate, Chichester, West Sussex, PO19 8SQ, United Kingdom: John Wiley and Sons, 2012.

[19]   A. Brandon, "CyberQuad: Best of both worlds UAV designed for urban reconnaissance," New Atlas, December 22, 2009. [Online]. Available: https://newatlas.com/cyberquad-uav/13652/

[20]   D. Rogers, "AeroViroment RQ-11 Raven," U.S. Air Force, July 28, 2006. [Online]. Available: http://www.af.mil/shared/media/photodb/photos/060801-F-0000D-002.jpg

[21]   A. Linnet, "Watchkeeper Remote Piloted Air System," British Army, April 25, 2013. [Online]. Available: http://www.defenceimagery.mod.uk/fotoweb/fwbin/download.dll /45153802.jpg

[22]   B. Zapka, "Global Hawk," U.S. Air Force, March 01, 2007. [Online]. Available: http://www.af.mil/shared/media/photodb/photos/070301-F-9126Z-229.jpg

[23]   P. Bendezu, "De fiero mito a tecnologia de ultima generacion," Revista Oficial de la Fuerza Aérea del Perú - Edición Nº518, May 2017. [Online]. Available: https://issuu.com/fap.mil.pe/docs/revista_aviacion_518/13

[24]   General Atomics Aeronautical, Predator XP, 2015. [Online]. Available: http://www.ga-asi.com/predator-xp

[25]   Northrop Grumman, MQ-4C Triton, 2016. [Online]. Available: http://www.northropgrumman.com/Capabilities/Triton/Pages/default.aspx

[26]   Alex Evers, "MQ-4C Triton flight testing," U.S. Navy, March 22, 2013. [Online]. Available: https://www.flickr.com/photos/usnavy/8906719846/

[27]   C. Honsberg and S. Bowden, "Absorption Coefficient," Photovoltaics Education Website, 2019. [Online]. Available: https://www.pveducation.org/pvcdrom/lead-acid-batteries/characteristics-of-lead-acid-batteries

[28]   R. Liu, L. Zhang, X.Sun, H Liu and J. Zhang, Eds., *Electrochemical Technologies for Energy Storage and Conversion.* Boschstr. 12, 69469 Weinheim, Germany: WILEY-VCH Verlag GmbH & Co. KGaA, 2012.

[29]   Clean Energy Institute, "Lithium-Ion Battery," The University of Washington. [Online]. Available: https://www.cei.washington.edu/education/science-of-solar/battery-technology/

[30]   B. Williams, "Lithium Iron Batteries for Energy Storage," Iron Edison Battery Company, June 13, 2019. [Online]. Available: https://www.altenergymag.com/article/2019/06/lithium-iron-batteries-for-energy-storage/31149

[31]   N. Kularatna, School of Engineering, The University of Waikato Hamilton, New Zealand *Energy Storage Devices for Electronic Systems Rechargeable Batteries and Supercapacitors*. 32 Jamestown Road, London NW1 7BY, UK: ELSEVIER.

[32]   "Atmospheric Effects on Lasers," class notes for Atmospheric Propagation, Dept. of Physics, Naval Postgraduate School, Monterey, CA, USA, fall 2018.

[33]   "Atmospheric Attenuation," class notes for Photonics & Electro-Optics, Dept. of Physics, Naval Postgraduate School, Monterey, CA, USA, summer 2019.

[34]   C. A. Romero, "Feasibility of high energy lasers for interdiction activities," M.S. thesis, Dept. of Applied Physics, NPS, Monterey, CA, USA, 2017. [Online]. Available: https://calhoun.nps.edu/handle/10945/56792

[35]   D. Sands, Pulsed Laser Heating and Melting, Heat Transfer, Engineering Applications, V. Vikhrenko, Ed. Rijeka, Croatia: InTeck, 2011.

[36]   J. Xie and A. Kar, "Mathematical modeling of melting during laser materials processing," Journal of Applied Physics, vol. 81, no. 7, pp. 3015–3022, 1997. Available: https://doi.org/10.1063/1.364336

[37]   S. B. Carr, "The Aerosol Models in MODTRAN: Incorporating Selected Measurements from Northern Australia," DSTO Defence Science and Technology Organisation, Edinburgh South Australia 5111 Australia, December 2005.

[38]   K. Cohn, "Linear atmospheric propagation effects," unpublished.

[39]   Office of the United States Attorney Southern District of California. [Online]. Available: https://www.nbcsandiego.com/multimedia/Photos-3-South-American-Men-Convicted-of-Trafficking-28M-in-Cocaine-by-Sea-508721261.html

[40]   "DE Overview," class notes for Electric Ship Weapon Systems, Dept. of Physics, Naval Postgraduate School, Monterey, CA, USA, fall 2019.

[41]   "The world's top combat drones," Army-Technology. Accessed Nov 25, 2019. [Online]. Available: https://www.army-technology.com/uncategorised/top-combat-drones/

[42]   A. Lionis, "Experimental design of a UCAV-based high-energy laser weapon," M.S. thesis, Dept. of Applied Physics, NPS, Monterey, CA, USA, 2016. [Online]. Available: https://calhoun.nps.edu/handle/10945/51574

[43]   Globalsecurity.org, "High Energy Laser Area Defense System (HELLADS)." [Online]. Available: https://www.globalsecurity.org/military/systems/aircraft/systems/hellads.htm.

[44]   Sam LaGrone, "Navy Ready to 'Burn the Boats' with 2021 Laser Installation on a Destroyer," US. Naval Institute USNI News, Mar. 20, 2019. [Online]. Available: https://news.usni.org/2019/03/20/navy-ready-burn-boats-2021-laser-installation-destroyer

INITIAL DISTRIBUTION LIST

1. Defense Technical Information Center
    Ft. Belvoir, Virginia

2. Dudley Knox Library
    Naval Postgraduate School
    Monterey, California